

Influence of profile shape on the diocotron instability in a non-neutral plasma column

Cite as: Physics of Plasmas 5, 3497 (1998); <https://doi.org/10.1063/1.873067>

Submitted: 23 April 1998 . Accepted: 26 June 1998 . Published Online: 21 September 1998

Ronald C. Davidson, and Gian Marco Felice



View Online



Export Citation

ARTICLES YOU MAY BE INTERESTED IN

[Diocotron Instability in a Cylindrical Geometry](#)

The Physics of Fluids **8**, 1288 (1965); <https://doi.org/10.1063/1.1761400>

[Diocotron Instability in Plasmas and Gas Discharges](#)

Journal of Applied Physics **37**, 602 (1966); <https://doi.org/10.1063/1.1708223>

[Compressional effects in nonneutral plasmas, a shallow water analogy and \$m=1\$ instability](#)

Physics of Plasmas **6**, 3744 (1999); <https://doi.org/10.1063/1.873637>

NEW

AVS Quantum Science

A new interdisciplinary home for impactful quantum science research and reviews

Co-Published by

NOW ONLINE

Influence of profile shape on the diocotron instability in a non-neutral plasma column

Ronald C. Davidson and Gian Marco Felice

Plasma Physics Laboratory, Princeton University, Princeton, New Jersey, 08543

(Received 23 April 1998; accepted 26 June 1998)

In this paper we examine theoretically the influence of density profile shape on the diocotron instability in a cylindrical, low-density ($\omega_{pe}^2 \ll \omega_{ce}^2$) non-neutral electron plasma column confined radially by a uniform axial magnetic field $B_0 \hat{\mathbf{e}}_z$. The analysis assumes electrostatic flute perturbations ($\partial/\partial z = 0$) about an axisymmetric equilibrium density profile $n_e^0(r)$, where $r = (x^2 + y^2)^{1/2}$ is the radial distance from the column axis. Two classes of density profiles with inverted population in radius r are considered. These are the following: (a) a *step-function* density profile with uniform density $\hat{n}_e \cdot \Delta$ in the column interior $0 \leq r < r_b^-$, and uniform density \hat{n}_e in an outer annular region $r_b^- < r < r_b^+$; and (b) a *continuously-varying* density profile of the form $n_e^0(r) = \hat{n}_e(\Delta + r^2/r_b^2)(1 - r^2/r_b^2)^2$ over the interval $0 \leq r < r_b$. Here, \hat{n}_e , r_b^- , r_b^+ and r_b are positive constants, and the dimensionless parameter Δ measures the degree of ‘‘hollowness’’ of the equilibrium density profile $n_e^0(r)$. Detailed linear stability properties are calculated for a wide range of system parameters, including values of the ‘‘filling factor’’ Δ , radial location r_w of the cylindrical conducting wall, azimuthal mode number l , etc. As a general remark, in both cases, it is found that small increases in Δ from the value $\Delta = 0$ (corresponding to the strongest diocotron instability) can have a large effect on the growth rate and detailed properties of the instability. In addition, for the step-function density profile, the instability tends to be algebraic in nature and have a large growth rate in the unstable region of parameter space, whereas for the continuously-varying density profile, the instability is typically much weaker and involves a narrow class of resonant particles at radius $r = r_s$ satisfying the resonance condition $\omega_r - l\omega_E(r_s) = 0$. Here, $\omega_r = Re \omega$ is the real oscillation frequency, and $\omega_E(r) = -cE_r^0(r)/rB_0$ is the equilibrium $\mathbf{E}^0 \times B_0 \hat{\mathbf{e}}_z$ rotation velocity of the plasma column. © 1998 American Institute of Physics. [S1070-664X(98)00810-6]

I. INTRODUCTION

The diocotron instability,¹ first examined theoretically by MacFarlane and Hay,² and Levy *et al.*,^{3–5} and observed in early experiments by Kyhl and Webster,^{6,7} and Kapetanakis *et al.*,⁸ is perhaps the most ubiquitous instability in a low-density ($\omega_{pe}^2 \ll \omega_{ce}^2$) non-neutral electron plasma column confined radially by a uniform axial magnetic field $B_0 \hat{\mathbf{e}}_z$. To briefly summarize, the diocotron instability is driven by a sufficiently strong shear in the angular $\mathbf{E}^0 \times B_0 \hat{\mathbf{e}}_z$ rotation velocity, $\omega_E(r) = -cE_r^0(r)/rB_0$, of the plasma column. Here, $r = (x^2 + y^2)^{1/2}$ is the radial distance from the column axis, and $E_r^0(r)$ is the equilibrium radial electric field determined self-consistently from Poisson’s equation in terms of the equilibrium density profile $n_e^0(r)$ (assumed axisymmetric). Whenever the density profile has an inverted population as a function of the radial coordinate r (an off-axis density maximum), the sign of

$$\frac{\partial}{\partial r} \frac{1}{r} \frac{\partial}{\partial r} [r^2 \omega_E(r)],$$

changes over the radial extent of the plasma column, and the shear in the angular flow velocity can provide the free energy to drive the Kelvin–Helmholtz-like instability known as the *diocotron instability*. Indeed, it can be shown that a *sufficient condition for stability*^{1,9–12} for small-amplitude electrostatic

flute perturbations ($\partial/\partial z = 0$) is that $n_e^0(r)$, or equivalently, $r^{-1}(\partial/\partial r)[r^2 \omega_E(r)]$, be a monotonically decreasing function of radius r . While detailed electrostatic stability properties have been calculated theoretically for a few simple choices of density profile $n_e^0(r)$, such as a hollow step-function annulus,^{1,3} or weak resonant versions^{1,9} of the diocotron instability, there has not been a systematic analysis of properties of the diocotron instability as a function of the shape of the density profile $n_e^0(r)$. Nonetheless, over the past decade, experimental studies^{13–18} of the diocotron instability, and related investigations of diocotron-like modes and vortex formation and merging have become increasingly sophisticated. Therefore, in the present analysis, we present a systematic analysis of the electrostatic eigenvalue equation¹ to determine the detailed influence of profile shape on the diocotron instability, at least for two classes of equilibrium density profiles $n_e^0(r)$ with an inverted population in radius r .

The organization of this paper is the following. The assumptions and theoretical model are discussed in Sec. II, and detailed stability properties are calculated in Sec. III for two choices of equilibrium density profile $n_e^0(r)$. These are the following: (a) a *step-function* density profile [Eq. (7)] with uniform density $\hat{n}_e \cdot \Delta = \text{const}$ in the column interior $0 \leq r < r_b^-$, and uniform density $\hat{n}_e = \text{const}$ in an outer annular region $r_b^- < r < r_b^+$; and (b) a *continuously-varying* density

profile [Eq. (9)] of the form $n_e^0(r) = \hat{n}_e(\Delta + r^2/r_b^2)(1 - r^2/r_b^2)^2$ over the interval $0 \leq r < r_b$. Here, \hat{n}_e , r_b^- , r_b^+ and r_b are positive constants, a perfectly conducting wall is located at radius $r = r_w$ and the dimensionless parameter Δ measures the degree of ‘‘hollowness’’ of the equilibrium density profile $n_e^0(r)$. Detailed linear stability properties are calculated in Sec. III for a wide range of system parameters, including values of the ‘‘filling factor’’ Δ , radial location r_w of the cylindrical conducting wall, azimuthal mode number l , etc. As a general remark, in both cases, it is found that small increases in Δ from the value $\Delta = 0$ (corresponding to the strongest diocotron instability) can have a large effect on the growth rate and detailed properties of the instability. In addition, for the step-function density profile in Eq. (7), the instability tends to be algebraic in nature and have a large growth rate in the unstable region of parameter space, whereas for the continuously-varying density profile in Eq. (9), the instability is typically much weaker and involves a narrow class of *resonant* particles at radius $r = r_s$ satisfying the resonance condition $\omega_r - l\omega_E(r_s) = 0$ in Eq. (42). Here, $\omega_r = Re \omega$ is the real oscillation frequency.

As a final point, although the present analysis is restricted to the diocotron instability for low-density non-neutral plasma with $\omega_{pe}^2(r) \ll \omega_{ce}^2$, it should be emphasized that detailed stability behavior and mode oscillation properties also exhibit a sensitive dependence on density profile shape at conditions approaching Brillouin flow ($\omega_{pe}^2/\omega_{ce}^2 \rightarrow 1$) in magnetically-insulated diode geometry.^{19,20} In this case, as shown by Kaup and Thomas,²⁰ the frequency characteristics of the magnetron mode are modified significantly when the density profile differs from a simple step-function profile.

II. ASSUMPTIONS AND THEORETICAL MODEL

We consider here a cylindrical low-density ($\omega_{pe}^2 \ll \omega_{ce}^2$) non-neutral electron plasma confined radially by a uniform axial magnetic field $B_0 \hat{e}_z$. Equilibrium properties are assumed to be azimuthally symmetric ($\partial/\partial\theta = 0$) about the column axis and have negligible spatial variation in the axial direction ($\partial/\partial z = 0$). For low-frequency electrostatic flute perturbations of the form $\delta\Phi(r, \theta, t) = \sum_l \delta\Phi_l(r) \exp(il\theta - i\omega t)$, the eigenvalue equation can be expressed as^{1,3}

$$\frac{1}{r} \frac{\partial}{\partial r} r \frac{\partial}{\partial r} \delta\Phi_l - \frac{l^2}{r^2} \delta\Phi_l = - \frac{l}{r\omega_{ce}} \frac{\partial\omega_{pe}^2}{\partial r} \frac{\delta\Phi_l}{[\omega - l\omega_E(r)]}. \quad (1)$$

Here, l is the azimuthal mode number, ω is the complex oscillation frequency, $\omega_{ce} = eB_0/m_e c$ is the electron cyclotron frequency and $\omega_{pe}^2(r) = 4\pi n_e^0(r)e^2/m_e$ is the electron plasma frequency-squared, where $n_e^0(r)$ is the equilibrium electron density profile, and $r = (x^2 + y^2)^{1/2}$ is the radial distance from the axis of symmetry. In Eq. (1) and related definitions, $-e$, m_e and c are the electron charge, electron mass and speed of light *in vacuo*, respectively, and $\omega_E(r) = -cE_r^0(r)/rB_0$ is the equilibrium $\mathbf{E}^0 \times B_0 \hat{e}_z$ angular rotation velocity determined self-consistently in terms of $n_e^0(r)$ from the equilibrium Poisson equation,

$$\frac{1}{r} \frac{\partial}{\partial r} [r^2 \omega_E(r)] = \frac{\omega_{pe}^2(r)}{\omega_{ce}}. \quad (2)$$

Over the years, Eq. (1) has been extensively analyzed for the case of the diocotron instability in an annular electron layer,^{1,3,5} surface oscillations on a uniform density plasma column,¹ stable $l = 1$ oscillation in a non-neutral plasma column with general density profile $n_e^0(r)$,^{1,4} and the resonant diocotron instability^{1,9,11} driven by weak shear in the angular velocity profile and gentle gradient $\partial\omega_{pe}^2/\partial r$ in the density profile. Indeed, even a sufficient condition for stability^{1,9-11} has been derived for general density profile $n_e^0(r)$ that decreases (or increases) monotonically as a function of radius r . Nonetheless, with the few exceptions noted above, there is a paucity of detailed stability results that have been obtained from Eq. (1) that illustrate the sensitivity of stability properties to the detailed shape of the equilibrium profiles for $n_e^0(r)$ and $\omega_E(r)$.

In the present analysis, we examine the eigenvalue equation (1) for the class of density profiles $n_e^0(r)$ which have an inverted population as a function of radius r (i.e., profiles with an off-axis density maximum). Depending on the ‘‘hollowness’’ of the density profile, the corresponding shear in the angular velocity profile $\omega_E(r)$ [Eq. (2)] can provide the free energy to drive the well-known diocotron instability. In this regard, it is important to recognize that density profiles $n_e^0(r)$ which are monotonically decreasing functions of radius r , will *not* give rise to instability with $\gamma = Im(\omega) > 0$. This readily follows from Eq. (1) upon multiplying by $r\delta\Phi_l^*$ and integrating from $r = 0$ to $r = r_w$. Here, it is assumed that a perfectly conducting cylindrical wall is located at radius $r = r_w$, in which case the perturbed potential amplitude $\delta\Phi_l(r)$ satisfies the boundary condition

$$\delta\Phi_l(r = r_w) = 0. \quad (3)$$

Expressing $\omega = \omega_r + i\gamma$, and integrating the first term in Eq. (1) by parts with respect to r , we obtain¹

$$0 = D(\omega_r + i\gamma) = \int_0^{r_w} dr r \left\{ \left| \frac{\partial}{\partial r} \delta\Phi_l \right|^2 + \frac{l^2}{r^2} |\delta\Phi_l|^2 - \frac{l}{r\omega_{ce}} \frac{1}{\omega_r - l\omega_E(r) + i\gamma} \frac{\partial\omega_{pe}^2}{\partial r} |\delta\Phi_l|^2 \right\}. \quad (4)$$

The factors $|\partial/\partial r \delta\Phi_l|^2$ and $|\delta\Phi_l|^2$ in Eq. (4) are manifestly real. Therefore, setting real and imaginary parts of Eq. (4) separately equal to zero gives

$$0 = \int_0^{r_w} dr r \left\{ \left| \frac{\partial}{\partial r} \delta\Phi_l \right|^2 + \frac{l^2}{r^2} |\delta\Phi_l|^2 - \frac{l}{r\omega_{ce}} \frac{[\omega_r - l\omega_E(r)]}{[\omega_r - l\omega_E(r)]^2 + \gamma^2} \frac{\partial\omega_{pe}^2}{\partial r} |\delta\Phi_l|^2 \right\}, \quad (5)$$

and

$$0 = \gamma \frac{1}{\omega_{ce}} \int_0^{r_w} dr \frac{1}{[\omega_r - l\omega_E(r)]^2 + \gamma^2} \frac{\partial\omega_{pe}^2}{\partial r} |\delta\Phi_l|^2. \quad (6)$$

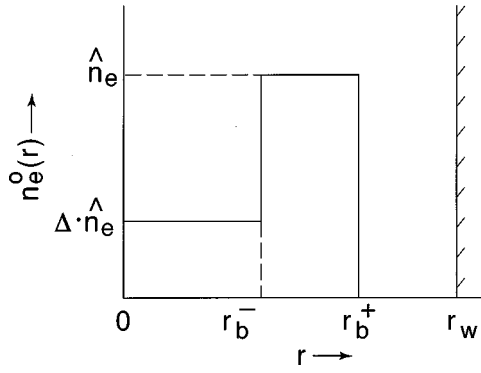


FIG. 1. Density profile $n_e^0(r)$ plotted versus radius r for the *step-function* profile in Eq. (7).

In circumstances where $\partial\omega_{pe}^2/\partial r$ does not change sign over the interval $0 \leq r \leq r_w$, the only solution to Eq. (6) corresponds to a zero growth rate with $\gamma = \text{Im } \omega = 0$. By the same token, it follows from Eq. (6) that a *necessary condition for instability* (solutions with $\gamma = \text{Im } \omega > 0$) is that $\partial\omega_{pe}^2/\partial r$ change sign over the interval $0 \leq r \leq r_w$.¹

The present stability analysis of Eq. (1) (Sec. III) focuses on two classes of equilibrium profiles with inverted population. The first is the *step-function* density profile specified by (Fig. 1)

$$n_e^0(r) = \begin{cases} \Delta \cdot \hat{n}_e = \text{const}, & 0 \leq r < r_b^-, \\ \hat{n}_e = \text{const}, & r_b^- < r < r_b^+, \\ 0, & r_b^+ < r \leq r_w. \end{cases} \quad (7)$$

Here, the (positive) dimensionless parameter Δ is a measure of the electron density depression inside the annulus $r_b^- < r < r_b^+$, with $\Delta = 1$ corresponding to a flat density profile extending from $r = 0$ to $r = r_b^+$, and $\Delta = 0$ corresponding to zero electron density in the region $0 \leq r < r_b^-$. An important physical quantity is the number of electrons per unit axial length of the plasma column defined by $N_e = 2\pi \int_0^{r_w} dr r n_e^0(r)$. For the equilibrium density profile in Eq. (7) it is readily shown that

$$N_e = \pi r_b^{+2} \hat{n}_e \left[1 - (1 - \Delta) \left(\frac{r_b^-}{r_b^+} \right)^2 \right]. \quad (8)$$

In Sec. III, it will be useful to eliminate \hat{n}_e in favor of N_e , and examine stability properties for a fixed amount of plasma (N_e) but variable profile shape parameters Δ , r_b^-/r_b^+ and r_b^+/r_w .

The second class of equilibrium profiles considered in Sec. III has continuous density variation over the radial extent of the plasma column. In particular, we consider the *continuously-varying* density profile $n_e^0(r)$ specified by (Fig. 2)

$$n_e^0(r) = \begin{cases} \hat{n}_e \left(\Delta + \frac{r^2}{r_b^2} \right) \left(1 - \frac{r^2}{r_b^2} \right)^2, & 0 \leq r < r_b, \\ 0, & r_b < r \leq r_w. \end{cases} \quad (9)$$

Here, $\hat{n}_e \Delta$ is the density on-axis ($r = 0$). For $\Delta \geq 1/2$, it is readily shown from Eq. (9) that $n_e^0(r)$ decreases monotonically

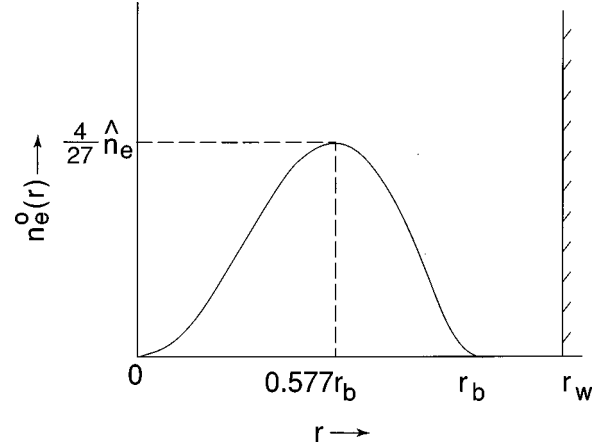


FIG. 2. Density profile $n_e^0(r)$ plotted versus radius r for the *continuously-varying* profile in Eq. (9). Here, $\Delta = 0$ is assumed.

cally over the entire interval from $r = 0$ to $r = r_b$. On the other hand, for $0 \leq \Delta < 1/2$ (the case of interest here), the density profile in Eq. (9) increases monotonically from the value $\hat{n}_e \Delta$ at $r = 0$, to the maximum value $n_{\text{max}} = (4/27) \hat{n}_e (1 + \Delta)^3$ at radius $r = r_{\text{max}} = [(1 - 2\Delta)/3]^{1/2} r_b$, and then decreases monotonically to zero (at $r = r_b$) over the interval $r_{\text{max}} \leq r \leq r_b$. The density profile in Eq. (9) is illustrated in Fig. 2 for the case where $\Delta = 0$. Finally, making use of $N_e = 2\pi \int_0^{r_w} dr r n_e^0(r)$, it is readily shown from Eq. (9) that

$$N_e = \pi r_b^2 \hat{n}_e \left(\frac{\Delta}{3} + \frac{1}{12} \right), \quad (10)$$

which can be used to express \hat{n}_e in terms of N_e , Δ and r_b .

Finally, for future reference, it will be useful in the analysis of the eigenvalue equation (1) to measure the (complex) eigenfrequency ω in units of the (real) frequency ω_1 for the $l = 1$ diocotron mode which is independent of the detailed profile shape for $n_e^0(r)$. Indeed, as first demonstrated by Levy,⁴ for azimuthal mode number $l = 1$ and *general density profile* $n_e^0(r)$, Eq. (1) supports a stable oscillatory solution ($\text{Im } \omega = 0$) with an eigenfunction given exactly by $\delta\Phi_{l=1} = \text{const} \times r[\omega - \omega_E(r)]$ over the interval $0 \leq r \leq r_w$. Enforcing the boundary condition $\delta\Phi_{l=1}(r = r_w) = 0$ then gives $\omega = \omega_E(r = r_w) \equiv \omega_1$, where

$$\omega_1 = \frac{2ec}{B_0 r_w^2} N_e. \quad (11)$$

Note from Eq. (11) that ω_1 is independent of the detailed profile shape, and depends only on the total amount of plasma (N_e), the magnetic field strength (B_0) and the conducting wall radius (r_w).

III. ANALYSIS OF EIGENVALUE EQUATION

We now make use of the eigenvalue equation (1) to investigate detailed electrostatic stability properties for the equilibrium density profiles $n_e^0(r)$ in Eqs. (7) and (9), both of which have inverted profiles and are expected to exhibit instability ($\text{Im } \omega > 0$), at least for modest values of the “filling factor” Δ (see Figs. 1 and 2).

A. Step-function density profile

For the step-function density profile in Fig. 1 and Eq. (7), we first evaluate the angular velocity profile $\omega_E(r)$. Substituting Eq. (7) into Eq. (2) readily gives

$$\omega_E(r) = \begin{cases} \Delta \hat{\omega}_d, & 0 \leq r < r_b^-, \\ \hat{\omega}_d \left[1 - (1 - \Delta) \left(\frac{r_b^-}{r} \right)^{2l} \right], & r_b^- < r < r_b^+, \end{cases} \quad (12)$$

over the radial extent ($0 \leq r < r_b^+$) of the plasma column. Here, $\hat{\omega}_d$ is an effective *diocotron frequency* defined in terms of \hat{n}_e by

$$\hat{\omega}_d \equiv \frac{\hat{\omega}_{pe}^2}{2\omega_{ce}} = \frac{2\pi\hat{n}_e ec}{B_0}. \quad (13)$$

Eliminating \hat{n}_e in favor of N_e and ω_1 by means of Eqs. (8) and (11), note that $\hat{\omega}_d$ can be expressed directly in terms of ω_1 according to

$$\hat{\omega}_d = \omega_1 \frac{(r_w/r_b^+)^2}{[1 - (1 - \Delta)(r_b^-/r_b^+)^2]}. \quad (14)$$

In the special case where $\Delta = 1$ (uniform density plasma column), it is clear from Eq. (12) that $\omega_E(r) = \hat{\omega}_d = \text{const}$ across the entire radial extent of the plasma column ($0 \leq r < r_b^+$). On the other hand, for $0 < \Delta < 1$, there can be a strong radial shear in $\omega_E(r)$, particularly when Δ is sufficiently small, which leads to unstable solutions to Eq. (1) with $\text{Im } \omega > 0$.

Substituting the step-function density profile (7) into the eigenvalue equation (1) gives

$$\begin{aligned} \frac{1}{r} \frac{\partial}{\partial r} r \frac{\partial}{\partial r} \delta\Phi_l - \frac{l^2}{r^2} \delta\Phi_l \\ = - \frac{2l}{r_b^-} \hat{\omega}_d (1 - \Delta) \frac{\delta\Phi_l(r_b^-)}{\omega - l\omega_E(r_b^-)} \delta(r - r_b^-) \\ + \frac{2l}{r_b^+} \hat{\omega}_d \frac{\delta\Phi_l(r_b^+)}{\omega - l\omega_E(r_b^+)} \delta(r - r_b^+). \end{aligned} \quad (15)$$

Here, $\hat{\omega}_d$ is defined in Eq. (13), and use has been made of Eq. (7) to express $\partial n_e^0(r)/\partial r = \hat{n}_e(1 - \Delta)\delta(r - r_b^-) - \hat{n}_e\delta(r - r_b^+)$. For the step-function density profile in Eq. (7), we note from the right-hand side of Poisson's equation (15) that the perturbed charge density $-e\delta n_l(r)$ is equal to zero except at the surfaces located at $r = r_b^-$ and $r = r_b^+$, where $\partial n_e^0(r)/\partial r$ is singular. Equation (15) is readily solved in the three regions: $0 \leq r < r_b^-$ (Region I); $r_b^- < r < r_b^+$ (Region II); and $r_b^+ < r \leq r_w$ (Region III). Denoting $\delta\Phi_- \equiv \delta\Phi_l(r = r_b^-)$ and $\delta\Phi_+ \equiv \delta\Phi_l(r = r_b^+)$, and enforcing regularity of $\delta\Phi_l(r)$ at $r = 0$, continuity of $\delta\Phi_l(r)$ over the interval $0 \leq r \leq r_w$ and $\delta\Phi_l(r = r_w) = 0$ at the conducting wall, we readily obtain the solution to Eq. (15) in the three regions. We find

$$\delta\Phi_l(r) = \begin{cases} \delta\Phi_l^I(r) = \delta\Phi_- \left(\frac{r}{r_b^-} \right)^l, & 0 \leq r < r_b^-, \\ \delta\Phi_l^II(r) = B r^l + \frac{C}{r^l}, & r_b^- < r < r_b^+, \\ \delta\Phi_l^III(r) = \delta\Phi_+ \frac{[(r_b^+/r)^l - (r_b^+/r_w)^l (r/r_w)^l]}{[1 - (r_b^+/r_w)^{2l}]}, & r_b^+ < r \leq r_w. \end{cases} \quad (16)$$

Here, to assure the continuity of $\delta\Phi_l(r)$ at $r = r_b^-$ and $r = r_b^+$, the constants B and C are related to the constants $\delta\Phi_- \equiv \delta\Phi_l(r = r_b^-)$ and $\delta\Phi_+ \equiv \delta\Phi_l(r = r_b^+)$ by the conditions

$$B = \frac{1}{(r_b^+)^{2l} - (r_b^-)^{2l}} [(r_b^+)^l \delta\Phi_+ - (r_b^-)^l \delta\Phi_-], \quad (17)$$

$$C = \frac{(r_b^-)^l (r_b^+)^l}{(r_b^+)^{2l} - (r_b^-)^{2l}} [-(r_b^-)^l \delta\Phi_+ + (r_b^+)^l \delta\Phi_-]. \quad (18)$$

The remaining boundary conditions at the surfaces $r = r_b^-$ and $r = r_b^+$ can be derived by operating on the eigenvalue equation (15) with $\int_{r_b^-(1-\epsilon)}^{r_b^+(1+\epsilon)} dr \dots$ and $\int_{r_b^+(1-\epsilon)}^{r_b^-(1+\epsilon)} dr \dots$, respectively, in the limit $\epsilon \rightarrow 0_+$. This gives

$$\begin{aligned} \left[\frac{\partial}{\partial r} \delta\Phi_l^II \right]_{r_b^-(1+\epsilon)} - \left[\frac{\partial}{\partial r} \delta\Phi_l^I \right]_{r_b^-(1-\epsilon)} \\ = - \frac{2l\hat{\omega}_d(1-\Delta)}{r_b^-} \frac{\delta\Phi_l(r_b^-)}{\omega - l\omega_E(r_b^-)}, \end{aligned} \quad (19)$$

$$\begin{aligned} \left[\frac{\partial}{\partial r} \delta\Phi_l^III \right]_{r_b^+(1+\epsilon)} - \left[\frac{\partial}{\partial r} \delta\Phi_l^II \right]_{r_b^+(1-\epsilon)} \\ = \frac{2l\hat{\omega}_d}{r_b^+} \frac{\delta\Phi_l(r_b^+)}{\omega - l\omega_E(r_b^+)}, \end{aligned} \quad (20)$$

where $\epsilon \rightarrow 0_+$, and $\delta\Phi_l^I(r)$, $\delta\Phi_l^II(r)$ and $\delta\Phi_l^III(r)$ are defined in Eq. (16). Equations (19) and (20) relate the discontinuity in perturbed radial electric field at the surfaces $r = r_b^-$ and $r = r_b^+$ to the perturbed charge density at those surfaces.

Substituting Eq. (16) into Eqs. (19) and (20), and eliminating the constants B and C in favor of the constants $\delta\Phi_- \equiv \delta\Phi_l(r = r_b^-)$ and $\delta\Phi_+ \equiv \delta\Phi_l(r = r_b^+)$, we obtain

$$\left[\frac{(1-\Delta)\hat{\omega}_d}{\omega - l\Delta\hat{\omega}_d} - \frac{1}{1 - (r_b^-/r_b^+)^{2l}} \right] \delta\Phi_- + \frac{(r_b^-/r_b^+)^l}{1 - (r_b^-/r_b^+)^{2l}} \delta\Phi_+ = 0, \quad (21)$$

$$\begin{aligned} \frac{2(r_b^-/r_b^+)^l}{1 - (r_b^-/r_b^+)^{2l}} \delta\Phi_- - \left[\frac{2\hat{\omega}_d}{\omega - l\hat{\omega}_d[1 - (1-\Delta)(r_b^-/r_b^+)^2]} \right. \\ \left. + \frac{1 + (r_b^+/r_w)^{2l}}{1 - (r_b^+/r_w)^{2l}} + \frac{1 + (r_b^-/r_b^+)^{2l}}{1 - (r_b^-/r_b^+)^{2l}} \right] \delta\Phi_+ = 0. \end{aligned} \quad (22)$$

Here, use has been made of Eq. (12) to express $\omega_E(r_b^-) = \Delta\hat{\omega}_d$ and $\omega_E(r_b^+) = \hat{\omega}_d[1 - (1-\Delta)(r_b^-/r_b^+)^2]$.

Equations (21) and (22) are of the form $a\delta\Phi_- + b\delta\Phi_+ = 0$ and $c\delta\Phi_- + d\delta\Phi_+ = 0$, where a , b , c and d are constant coefficients that depend on ω . The condition for a nontrivial solution with $\delta\Phi_- \neq 0$ and $\delta\Phi_+ \neq 0$ is given by $ad - bc = 0$, which plays the role of a dispersion relation that determines the complex oscillation frequency $\omega = \omega_r + i\gamma$ as a function of $\hat{\omega}_d$, Δ , r_b^-/r_b^+ , etc.

A simple limit in which to check Eqs. (21) and (22) is the special case where $\Delta = 1$, which corresponds to a uniform density profile with density \hat{n}_e extending from $r=0$ to $r=r_b^+$. Equation (21) gives $\delta\Phi_- = (r_b^-/r_b^+)^l \delta\Phi_+$ for $\Delta = 1$, and substitution into Eq. (22) then gives the simple result

$$\omega - (l-1)\hat{\omega}_d = \hat{\omega}_d (r_b^+/r_w)^{2l}, \quad \text{for } \Delta = 1. \quad (23)$$

Equation (23) is the expected result¹ for the case of a uniform step-function density profile extending from $r=0$ to $r=r_b^+$. Note from Eq. (23) that ω is purely real, corresponding to a stable oscillation. Moreover, for $l=1$ and $\Delta=1$, Eq. (23) reduces to $\omega = \hat{\omega}_d (r_b^+/r_w)^2 = \omega_1$, as expected [see Eq. (14)].⁴

We now return to Eqs. (21) and (22) for general values of Δ , r_b^-/r_b^+ , etc. Setting the two-by-two determinant of the coefficients of $\delta\Phi_-$ and $\delta\Phi_+$ in Eqs. (21) and (22) equal to zero, and rearranging terms, it is readily shown that

$$\left(\frac{r_b^-}{r_b^+} \right)^{2l} + \left[\frac{(1-\Delta)\hat{\omega}_d[1-(r_b^-/r_b^+)^{2l}]}{\omega - l\hat{\omega}_d} - 1 \right] \times \left[\frac{\hat{\omega}_d[1-(r_b^-/r_b^+)^{2l}]}{\omega - l\hat{\omega}_d[1-(1-\Delta)(r_b^-/r_b^+)^2]} + \frac{1-(r_b^-/r_w)^{2l}}{1-(r_b^+/r_w)^{2l}} \right] = 0. \quad (24)$$

Equation (24) can be cast into the form of a quadratic equation for $\omega/\hat{\omega}_d$. Some straightforward algebraic manipulation gives

$$(\omega/\hat{\omega}_d)^2 - 2\hat{b}(\omega/\hat{\omega}_d) + \hat{c} = 0, \quad (25)$$

where the constants \hat{b} and \hat{c} are defined by

$$\begin{aligned} 2\hat{b} = & l[1 + \Delta - (1-\Delta)(r_b^-/r_b^+)^2] - \{[1 - (r_b^+/r_w)^{2l}] \\ & - (1-\Delta)[1 - (r_b^-/r_w)^{2l}]\}, \\ \hat{c} = & l^2[1 - (1-\Delta)(r_b^-/r_b^+)^2]\Delta - \{l[1 - (r_b^+/r_w)^{2l}]\Delta \\ & - l[1 - (r_b^-/r_w)^{2l}](1-\Delta)[1 - (1-\Delta)(r_b^-/r_b^+)^2] \\ & + (1-\Delta)[1 - (r_b^-/r_b^+)^{2l}][1 - (r_b^+/r_w)^{2l}]\}. \end{aligned} \quad (27)$$

The solutions to Eq. (25) are given by

$$\frac{\omega}{\hat{\omega}_d} = \hat{b} \pm (\hat{b}^2 - \hat{c})^{1/2}. \quad (28)$$

Evidently, the necessary and sufficient condition for instability is

$$\hat{c} > \hat{b}^2. \quad (29)$$

Whenever the inequality in Eq. (29) is satisfied, the solutions to Eq. (28) occur in conjugate pairs, and the growth rate of

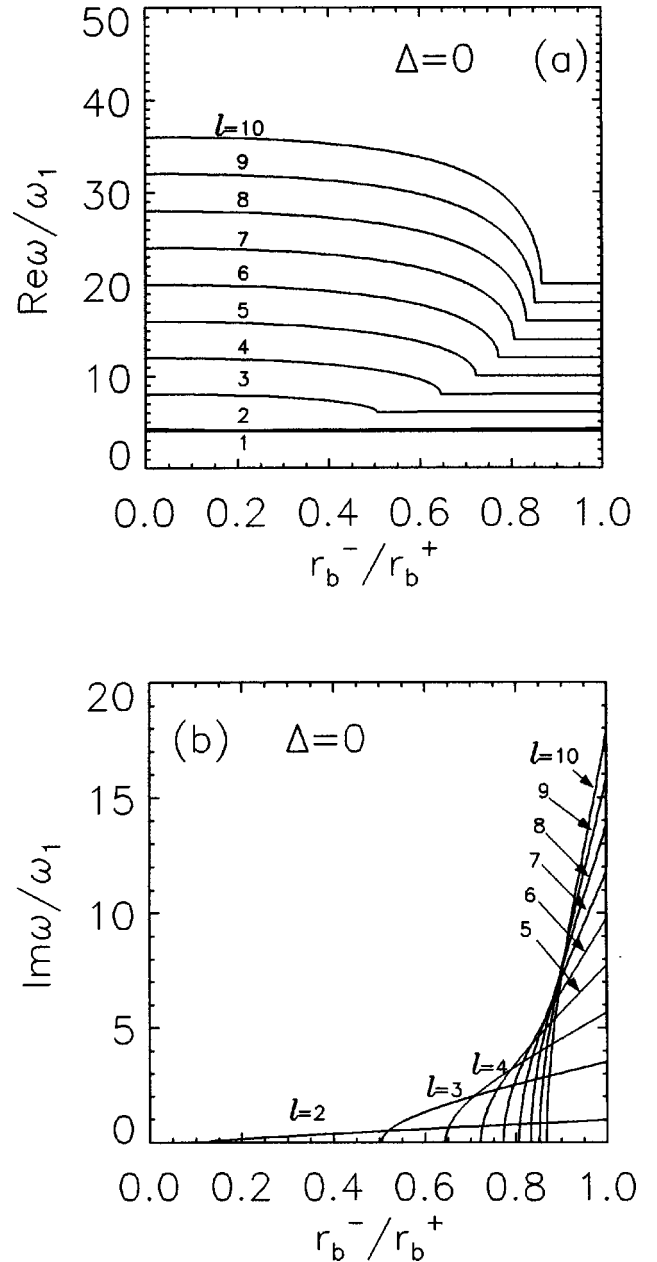


FIG. 3. Plots of (a) normalized real frequency $Re \omega / \omega_1$ and (b) normalized growth rate $Im \omega / \omega_1$ versus r_b^- / r_b^+ for the unstable (upper) branch in Eq. (28). Numerical results are presented for azimuthal mode numbers $l = 1, 2, \dots, 10$, assuming a fixed conducting wall radius with $r_b^+/r_w = 0.5$, and filling factor $\Delta = 0$ [see Eq. (7)].

the unstable branch is $Im \omega = +(\hat{c} - \hat{b}^2)^{1/2} \hat{\omega}_d > 0$, and the real frequency is $Re \omega = \hat{b} \hat{\omega}_d$. Of course, $Im \omega$ and $Re \omega$ can be expressed in units of the $l=1$ frequency ω_1 by means of Eq. (14). For azimuthal mode number $l=1$, and general values of Δ , r_b^-/r_b^+ and r_b^+/r_w , it is readily shown that the two solutions in Eq. (28) reduce to stable oscillations with frequency $\omega = \omega_1 (r_w/r_b^+)^2$ (upper sign) and $\omega = \omega_1$ (lower sign), where ω_d has been eliminated in favor of ω_1 by means of Eq. (14).^{1,4}

Typical numerical results for the unstable (upper) branch in Eq. (28) are illustrated in Figs. 3–5. Here, $Re \omega / \omega_1$ and $Im \omega / \omega_1$ are plotted versus r_b^- / r_b^+ for fixed values of the conducting wall location ($r_b^+/r_w = 0.5$) and values of filling

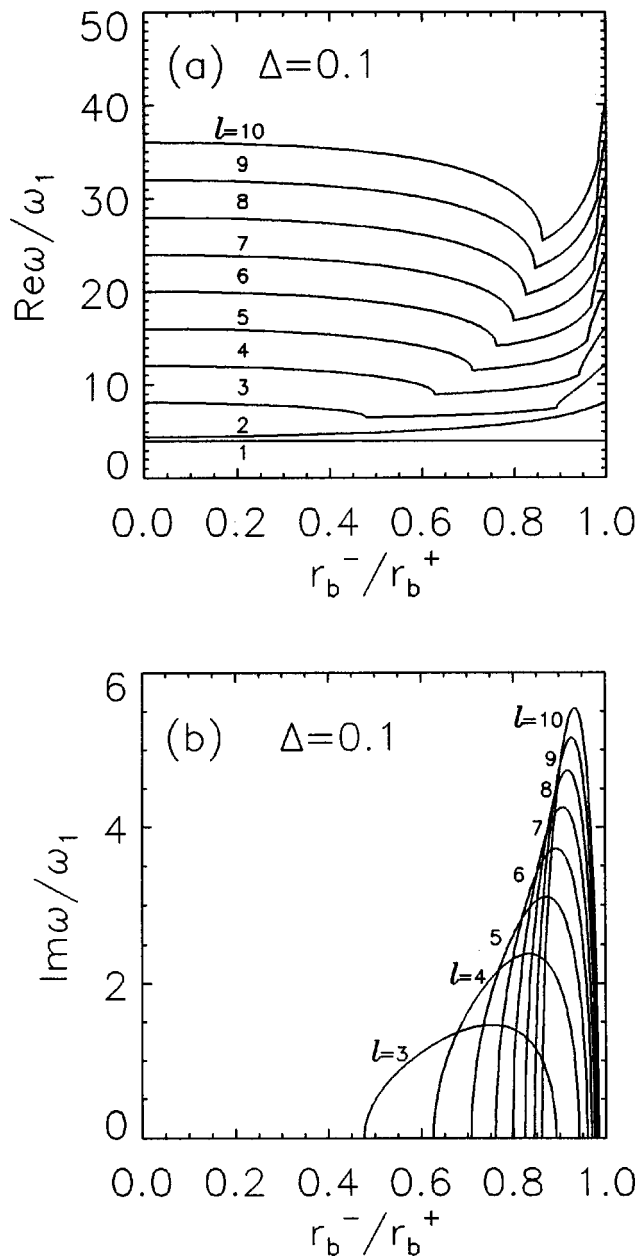


FIG. 4. Plots of (a) normalized real frequency $Re \omega / \omega_1$ and (b) normalized growth rate $Im \omega / \omega_1$ versus r_b^- / r_b^+ for the unstable (upper) branch in Eq. (28). Numerical results are presented for azimuthal mode numbers $l = 1, 2, \dots, 10$, assuming a fixed conducting wall radius with $r_b^+ / r_w = 0.5$, and filling factor $\Delta = 0.1$ [see Eq. (7)].

factor Δ corresponding to $\Delta = 0$ (Fig. 3), $\Delta = 0.1$ (Fig. 4) and $\Delta = 0.5$ (Fig. 5). The results in Figs. 3–5 are presented for azimuthal mode numbers $l = 1, 2, \dots, 10$. For $\Delta = 0$, as expected from previous analyses,^{1,3} it is evident from Fig. 3(b) that as the layer thickness is decreased (increasing values of r_b^- / r_b^+), the $l = 2$ mode is the first to go unstable, then the $l = 3$ mode, then $l = 4$, etc. Furthermore, the maximum growth rate is larger for larger l values, and occurs in the limit of a very thin annulus ($r_b^- / r_b^+ \rightarrow 1$).

Introducing even a *small* population of electrons in the interior region $0 \leq r < r_b^-$ can have a significant influence on stability properties. This is evident from Fig. 4, where $Re \omega / \omega_1$ and $Im \omega / \omega_1$ are plotted versus r_b^- / r_b^+ for the case

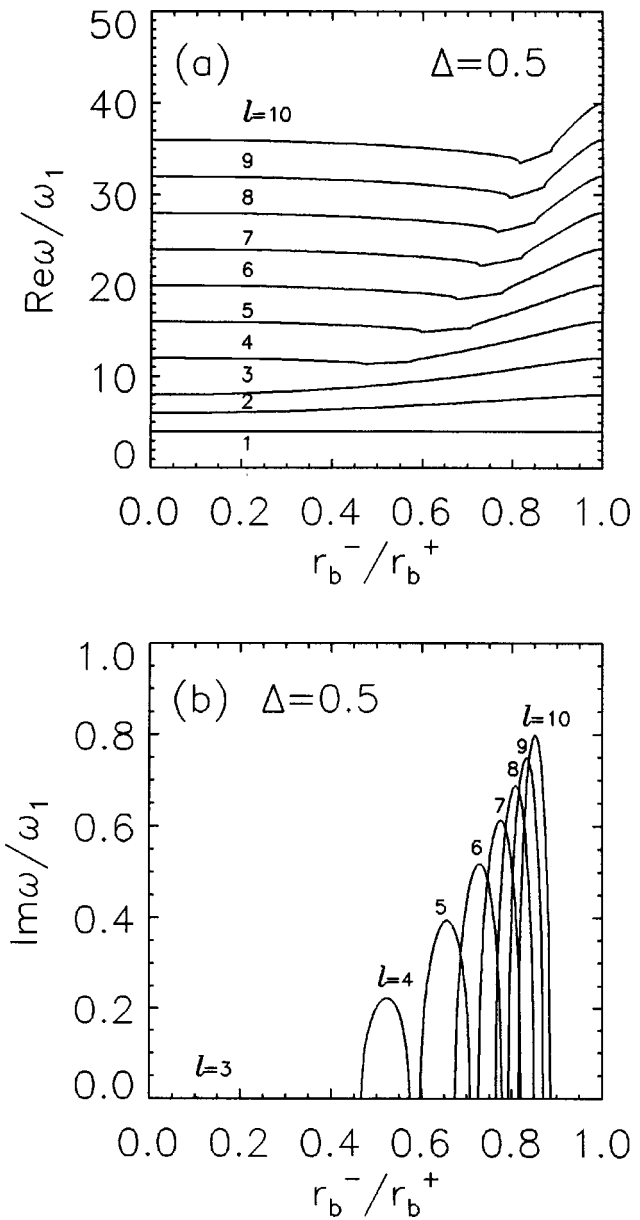


FIG. 5. Plots of (a) normalized real frequency $Re \omega / \omega_1$ and (b) normalized growth rate $Im \omega / \omega_1$ versus r_b^- / r_b^+ for the unstable (upper) branch in Eq. (28). Numerical results are presented for azimuthal mode numbers $l = 1, 2, \dots, 10$, assuming fixed conducting wall radius with $r_b^+ / r_w = 0.5$, and filling factor $\Delta = 0.5$ [see Eq. (7)].

where $\Delta = 0.1$. Comparing Figs. 4(b) and 3(b), several points are noteworthy. First, for $\Delta = 0.1$, the $l = 2$ mode is *not* unstable. Second, the maximum growth rates are reduced in Fig. 4(b) relative to Fig. 3(b). Finally, the bandwidth structure in Fig. 4(b) differs from that in Fig. 3(b), with each mode stabilizing ($Im \omega = 0$) for r_b^- / r_b^+ exceeding a certain critical value less than unity. For example, the $l = 3$ mode in Fig. 4(b) is unstable only in the range $0.47 < r_b^- / r_b^+ < 0.88$, and no longer extends to values of r_b^- / r_b^+ approaching unity as in Fig. 3(b). The stabilizing influence of introducing plasma in the interior region $0 \leq r < r_b^-$ is even more strongly evident in Fig. 5, where $Re \omega / \omega_1$ and $Im \omega / \omega_1$ are plotted versus r_b^- / r_b^+ for the case where $\Delta = 0.5$.

Detailed stability properties are readily calculated from

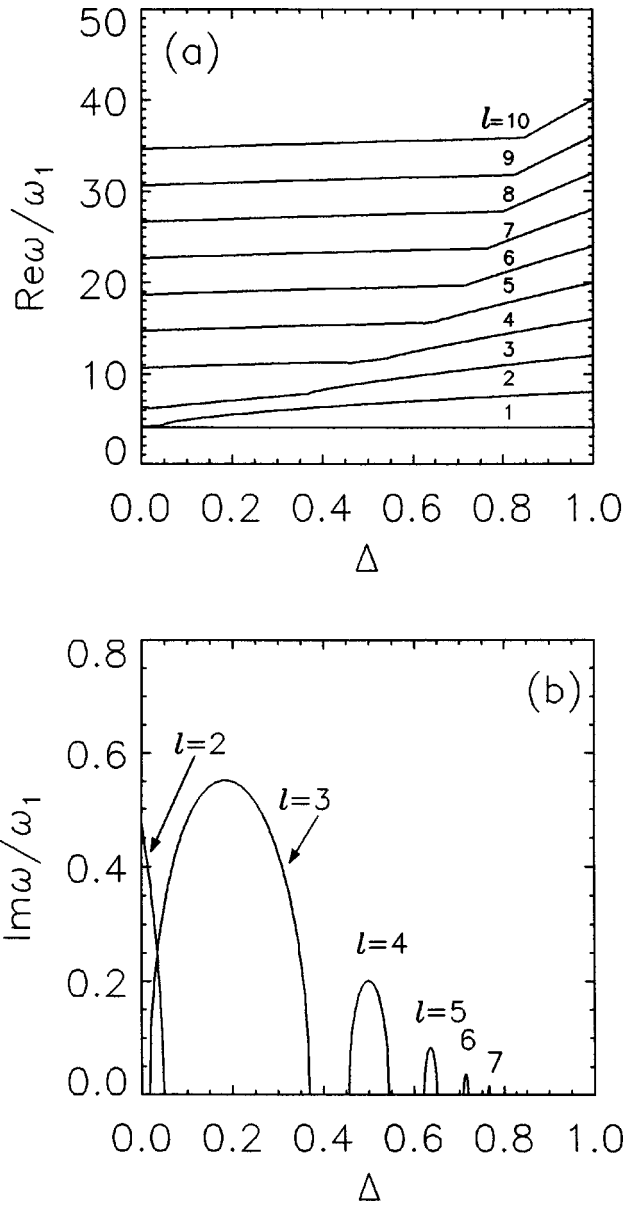


FIG. 6. Plots of (a) normalized real frequency $Re \omega / \omega_1$ and (b) normalized growth rate $Im \omega / \omega_1$ versus filling factor Δ for the unstable (upper) branch in Eq. (28). Numerical results are presented for azimuthal mode numbers $l = 1, 2, \dots, 10$, and fixed geometric factors $r_b^-/r_b^+ = 0.5$ and $r_b^+/r_w = 0.5$ [see Eq. (7)].

Eq. (28) as a function of the filling factor Δ for fixed values of the geometric factors r_b^-/r_b^+ and r_b^+/r_w . Typical numerical results are presented in Figs. 6 and 7, where $Re \omega / \omega_1$ and $Im \omega / \omega_1$ are plotted versus Δ for azimuthal mode numbers $l = 1, 2, \dots, 10$, and fixed value of $r_b^-/r_b^+ = 0.5$. The only difference between the two cases is the location of the conducting wall, with $r_b^+/r_w = 0.5$ in Fig. 6, and $r_b^+/r_w = 0.7$, in Fig. 7. The strong dependence of detailed stability behavior on Δ is evident from Figs. 6 and 7. First, at fixed values of r_b^-/r_b^+ and r_b^+/r_w , but varying Δ , the modes are *isolated from one another*, except for a modest overlap of the $l=2$ and $l=3$ modes over a relatively narrow range of Δ . For example, in Fig. 6(b), when $\Delta = 0.5$, only the $l=4$ mode is unstable, etc. Second, it is clear from Fig. 6(b) that the maxi-

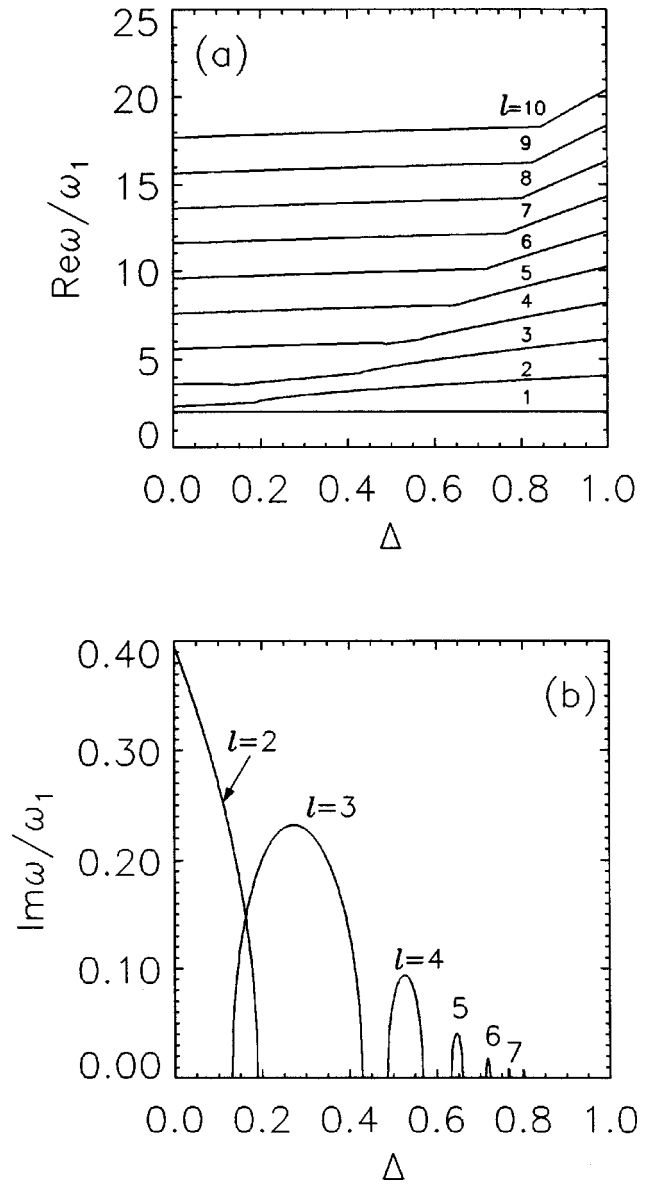


FIG. 7. Plots of (a) normalized real frequency $Re \omega / \omega_1$ and (b) normalized growth rate $Im \omega / \omega_1$ versus filling factor Δ for the unstable (upper) branch in Eq. (28). Numerical results are presented for azimuthal mode numbers $l = 1, 2, \dots, 10$, and fixed geometric factors $r_b^-/r_b^+ = 0.5$ and $r_b^+/r_w = 0.7$ [see Eq. (7)].

imum growth rate is a rapidly decreasing function of l for azimuthal mode numbers $l \geq 3$. Third, comparing Figs. 6(b) and 7(b), it is clear for each value of l that the maximum growth rate is reduced as the conducting wall is brought into closer proximity to the outer surface r_b^+ of the plasma. Here, keep in mind that $r_b^+/r_w = 0.5$ in Fig. 6, whereas $r_b^+/r_w = 0.7$ in Fig. 7.

Comparing the relative magnitudes of the $l=2$ and $l=3$ growth rates in Figs. 6(b) and 7(b), it is evident that the $l=2$ mode exhibits a special sensitivity to the location of the conducting wall. Indeed, careful examination of Eqs. (26)–(28) shows that as the conducting wall is removed to infinity ($r_b^+/r_w \rightarrow 0$), the growth rate of the $l=2$ mode reduces *exactly* to $Im \omega = 0$ for arbitrary values of Δ and r_b^-/r_b^+ . On the other hand, at fixed values of Δ and r_b^-/r_b^+ , the higher

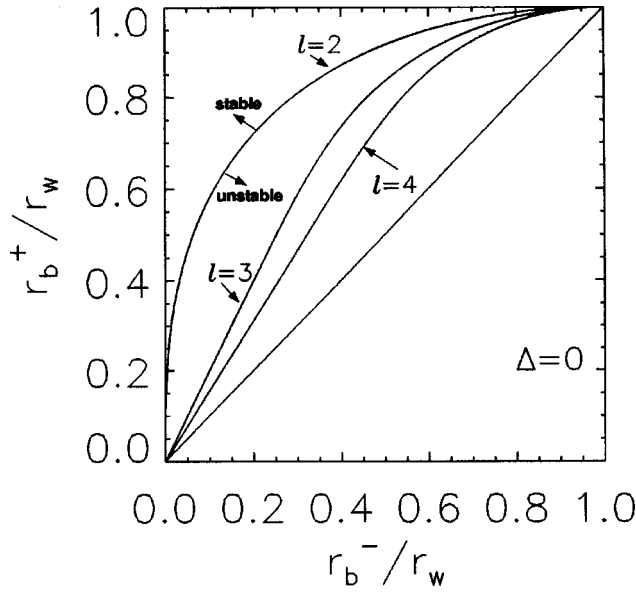


FIG. 8. Stability-instability contour plots of $\hat{b}^2 = \hat{c}$ obtained from Eqs. (26) and (27) in the parameter space $(r_b^-/r_w, r_b^+/r_w)$ for azimuthal mode numbers $l=2, 3, 4$, and filling factor $\Delta=0$.

mode numbers $l \geq 3$ continue to exhibit instability as the conducting wall is removed to infinity with $r_b^+/r_w \rightarrow 0$, at least in certain very narrow regions of the parameter space $(\Delta, r_b^-/r_b^+)$.

It is evident from Figs. 3–7 that detailed stability behavior exhibits a sensitive dependence on the dimensionless parameters Δ , r_b^-/r_b^+ and r_b^+/r_w for the choice of step-function density profile in Eq. (7). Moreover, the inequality $\hat{c} > \hat{b}^2$ in Eq. (29) is a necessary and sufficient condition for instability. Indeed the inequality $\hat{c} = \hat{b}^2$ can be used to generate contour plots in two-dimensional subspaces of the parameter space $(r_b^-/r_w, r_b^+/r_w, \Delta)$ that separate regions of instability ($\hat{c} > \hat{b}^2$ and $Im \omega > 0$) from regions of stable oscillations ($\hat{b}^2 > \hat{c}$ and $Im \omega = 0$). Typical numerical results are illustrated in Figs. 8–10, where stability-instability contours are plotted in the parameter space $(r_b^-/r_w, r_b^+/r_w)$. Because $r_b^+ \geq r_b^-$, only the regions above the 45-degree lines in Figs. 8–10 are physically allowed. Figure 8 corresponds to the case $\Delta=0$ first considered by Levy,³ and the contours are plotted for azimuthal mode numbers $l=2, 3$ and 4. Figure 8 is, of course, consistent with the stability behavior presented in Fig. 3. For example, at fixed value of r_b^+/r_w , as $r_b^-/r_b^+ = (r_b^-/r_w)(r_w/r_b^+)$ is increased, it follows from Fig. 8 that the $l=2$ mode is the first to go unstable, then the $l=3$ mode, then $l=4$, etc., which should be compared with the results in Fig. 3(b). As is evident from Figs. 9 and 10, and as would be expected from the quantitative stability results presented in Figs. 4–7, the stability-instability contours undergo a dramatic change in topology as Δ is increased from the $\Delta=0$ case shown in Fig. 8. This is illustrated for azimuthal mode number $l=2$ in Fig. 9 and for $l=3$ in Fig. 10, for several values of the filling factor $\Delta=0.1, 0.2, 0.3$ and 0.6. Comparing the $l=2$ contours in Figs. 8 and 9, it is clear that the $l=2$ contour detaches from the 45-degree line (r_b^+

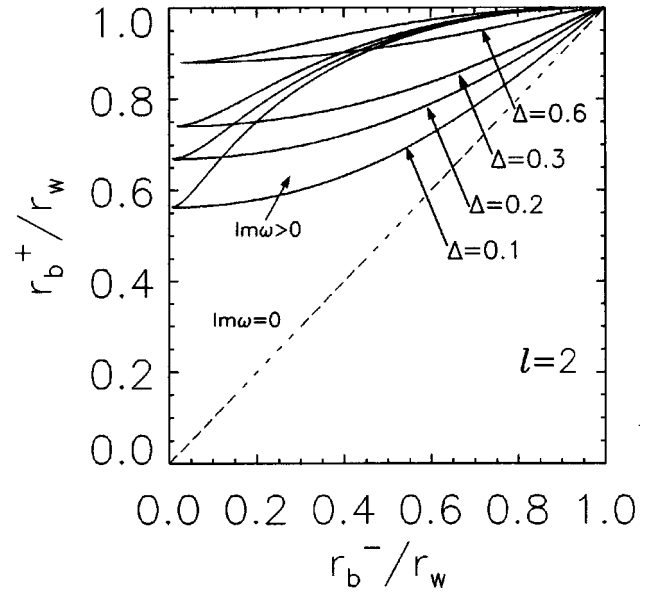


FIG. 9. Stability-instability contour plots of $\hat{b}^2 = \hat{c}$ obtained from Eqs. (26) and (27) in the parameter space $(r_b^-/r_w, r_b^+/r_w)$ for azimuthal mode number $l=2$, and filling factors $\Delta=0.1, 0.2, 0.3$ and 0.6.

$= r_b^-)$ when $\Delta \neq 0$, leading to regions of stability ($Im \omega = 0$) at both smaller and larger values of r_b^-/r_b^+ . (It is the regions *inside* the elongated loops in Fig. 9 that correspond to instability with $Im \omega > 0$.) Furthermore, from Fig. 9, the area of $(r_b^-/r_w, r_b^+/r_w)$ parameter space corresponding to instability ($Im \omega > 0$) becomes smaller and smaller as Δ is increased, and shifts to larger values of r_b^+/r_w . For azimuthal mode number $l=3$, it is evident from Fig. 10 that the stability-instability contour also detaches from the 45-degree line when $\Delta \neq 0$, although the shape and orientation of the unstable region is more complex than for the $l=2$ case shown in Fig. 9.

In concluding Sec. III A, we summarize briefly properties of the (complex) eigenfunction solution for $\delta\Phi_l(r)$ in Eq. (16). Here, the amplitude factors $\delta\Phi_- \equiv \delta\Phi_l(r=r_b^-)$ and $\delta\Phi_+ \equiv \delta\Phi_l(r=r_b^+)$ are related by Eqs. (21) and (22), where the complex oscillation frequency $\omega = \omega_r + i\gamma$ is determined self-consistently from the dispersion relation in Eq. (24), or equivalently, Eq. (25). Because of the $r^{\pm 1}$ dependences, we note from Eq. (16) that $\delta\Phi_l(r)$ is generally peaked (strongly so for large l -values) at the inner and outer surfaces of the step-function density profile at $r=r_b^-$ and $r=r_b^+$, respectively. Typical numerical results are illustrated in Fig. 11, where $Re \delta\Phi_l(r)$ and $Im \delta\Phi_l(r)$ are plotted versus radius r for azimuthal mode number $l=3$, filling factor $\Delta=0.1$ and geometric factors $r_b^-/r_b^+=0.7$ and $r_b^+/r_w=0.5$. This corresponds (approximately) to the maximum-growth-rate parameters for the unstable $l=3$ mode in Fig. 4. Without loss of generality, we pick the phase of the eigenfunction $\delta\Phi_l(r)$ for mode number $l=3$ so that $\delta\Phi_-$ is purely real, and plot $Re \delta\Phi_l(r)$ and $Im \delta\Phi_l(r)$, normalized in units of $\delta\Phi_-$, versus radius r in Fig. 11. Because $\omega = \omega_r + i\gamma = 6.7\omega_1 + i1.4\omega_1$ has nonzero real and imaginary parts determined from Eq. (25), it follows from Eqs. (21) and (22) that $\delta\Phi_+ = (2.57 + i0.074)\delta\Phi_-$ is also complex. As expected from

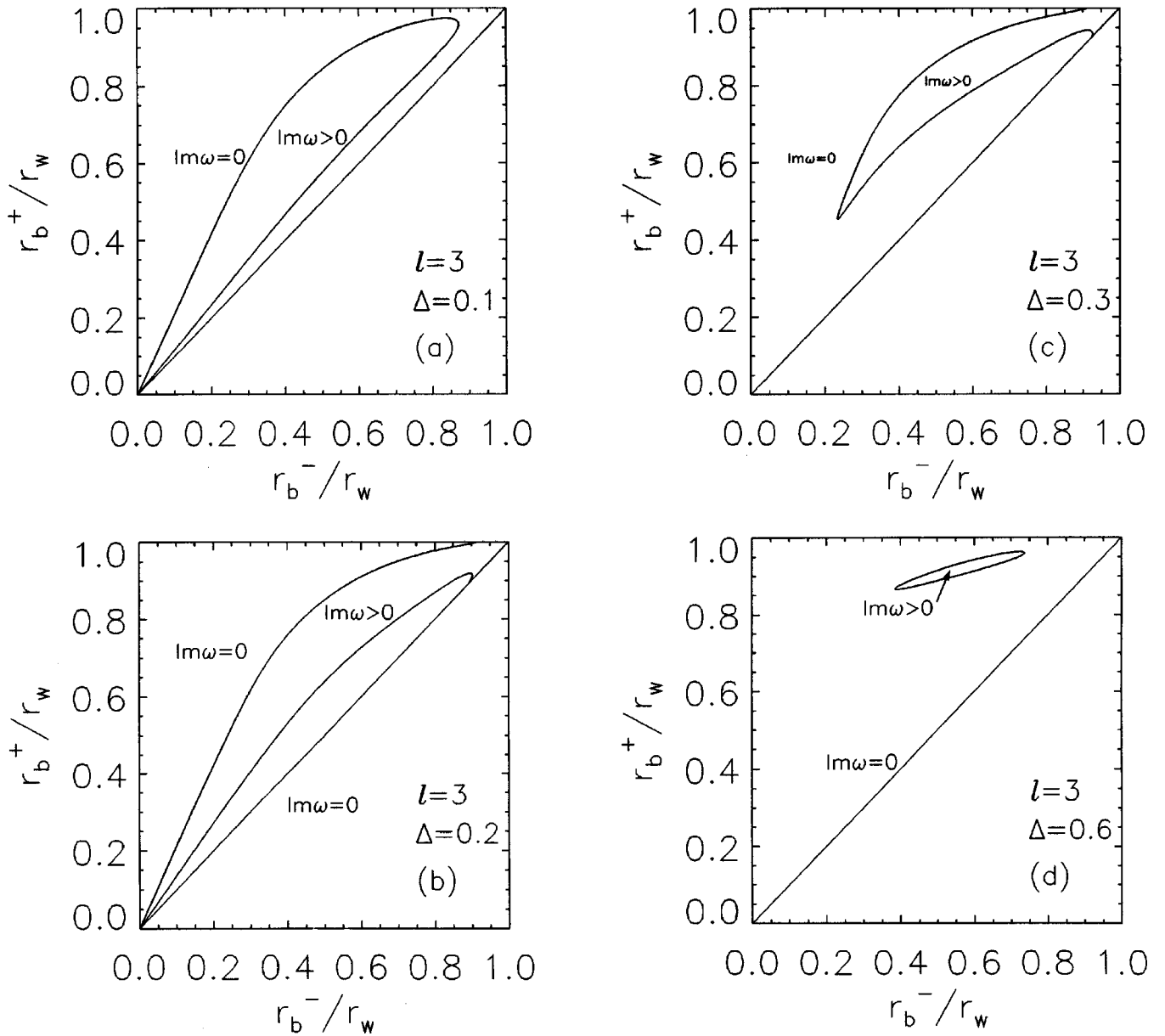


FIG. 10. Stability-instability contour plots of $\delta^2 = \hat{c}$ obtained from Eqs. (26) and (27) in the parameter space $(r_b^-/r_w, r_b^+/r_w)$ for azimuthal mode number $l=3$, and filling factors (a) $\Delta=0.1$, (b) $\Delta=0.2$, (c) $\Delta=0.3$ and (d) $\Delta=0.6$.

Eq. (16), the eigenfunction $\delta\Phi_l(r)$, plotted versus radius r in Fig. 11, develops both real and imaginary components in the interval $r_b^- < r \leq r_w$.

As a final point, the right-hand side of Eq. (15) is equal to $4\pi e \delta n_l(r)$, where $\delta n_l(r)$ is the perturbed density of electrons. For the step-function equilibrium density profile in Eq. (7), it is clear from Eq. (15) that the perturbed charge density is equal to zero everywhere except at the surfaces $r=r_b^-$ and $r=r_b^+$, where there are large (singular) perturbations in surface charge density, $\sigma_-(r_b^-) \equiv (2\pi r_b^-)^{-1}(-e) \int_{r_b^-(1-\epsilon)}^{r_b^-(1+\epsilon)} dr \times r \delta n_l(r)$ and $\sigma_+(r_b^+) \equiv (2\pi r_b^+)^{-1}(-e) \int_{r_b^+(1-\epsilon)}^{r_b^+(1+\epsilon)} dr r \delta n_l(r)$, where $\epsilon \rightarrow 0_+$. Without present algebraic details, which make use of Eqs. (21), (22) and (24), it can be shown that $\text{Re}[r_b^- \sigma_-(r_b^-)] + \text{Re}[r_b^+ \sigma_+(r_b^+)] = 0$ and $\text{Im}[r_b^- \sigma_-(r_b^-)]$

$+ \text{Im}[r_b^+ \sigma_+(r_b^+)] = 0$, which correspond to zero net perturbed charge density, i.e., $e \int_0^{r_w} dr r \delta n_l(r) = 0$, as expected.

B. Continuously-varying density profile

As a second example, we consider the continuously-varying density profile in Eq. (9) and Fig. 2. Here, $n_e^0(r)$ varies smoothly over the interval $0 \leq r < r_b$, and has an inverted population for sufficiently small values of $\Delta < 1/2$. Substituting Eq. (9) into Eq. (2) and integrating with respect to r gives the angular velocity profile

$$\omega_E(r) = \hat{\omega}_d \left[\Delta + \left(\frac{1}{2} - \Delta \right) \frac{r^2}{r_b^2} - \frac{1}{3} (2 - \Delta) \frac{r^4}{r_b^4} + \frac{1}{4} \frac{r^6}{r_b^6} \right],$$

$$0 \leq r < r_b, \quad (30)$$

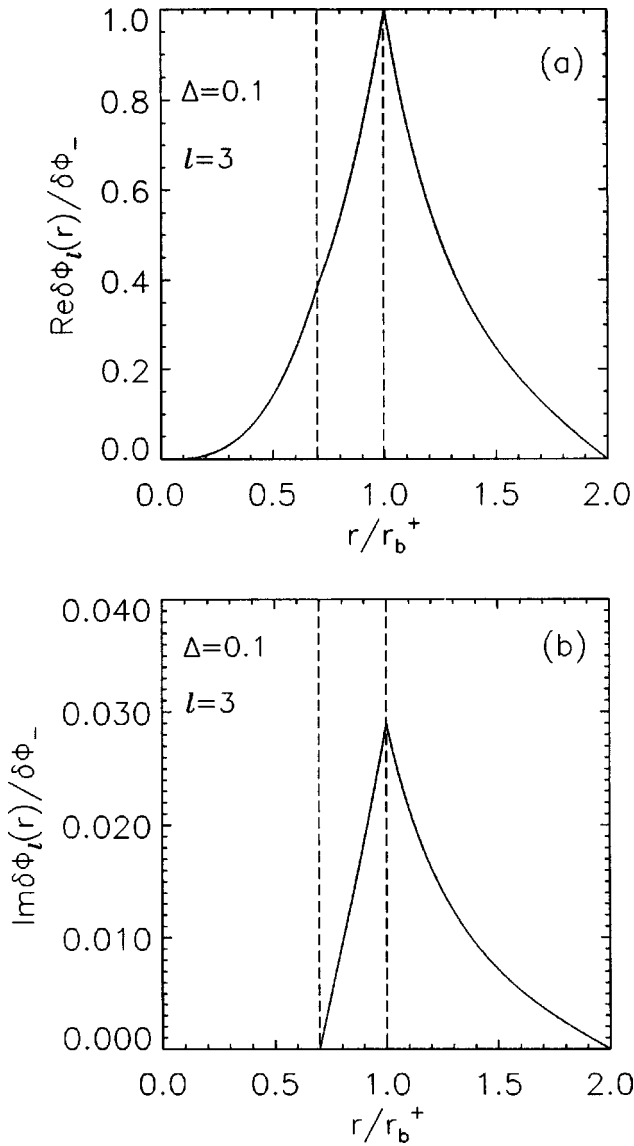


FIG. 11. A plot of the complex eigenfunction $\delta\Phi_l(r)$ versus radius r obtained from Eq. (16) for azimuthal mode number $l=3$, filling factor $\Delta=0.1$ and geometric factors $r_b^-/r_b^+=0.7$ and $r_b^+/r_w=0.5$. Here, we have taken $\delta\Phi_-$ to be real, and made use of Eqs. (21), (22) and (25) to determine the real and imaginary components of $\delta\Phi_+$.

where $\hat{\omega}_d \equiv \hat{\omega}_{pe}^2/2\omega_{ce} = 2\pi\hat{n}_e e c/B_0$. Here, $\hat{\omega}_d$ can be eliminated in favor of N_e and the $l=1$ diocotron frequency ω_1 by means of Eqs. (10) and (11). This gives

$$\hat{\omega}_d = \frac{r_w^2/r_b^2}{(\Delta/3 + 1/12)} \omega_1. \quad (31)$$

Plots of the normalized profiles for $\pi r_b^2 n_e^0(r)/N_e$ and $\omega_E(r)/\omega_1$ versus r/r_b calculated from Eqs. (9) and (30), respectively, are shown in Fig. 12 for several values of the dimensionless parameter Δ to illustrate the sensitive dependence of profile shape on Δ . Here, use has been made of Eqs. (10) and (31) to eliminate \hat{n}_e and $\hat{\omega}_d$ in favor of N_e and ω_1 .

For $n_e^0(r)$ specified by Eq. (9) and sufficiently small Δ , the shear in the angular velocity profile $\omega_E(r)$ defined in Eq. (30) is sufficiently large to drive the diocotron instability. For the equilibrium profiles in Eqs. (9) and (30), exact ana-

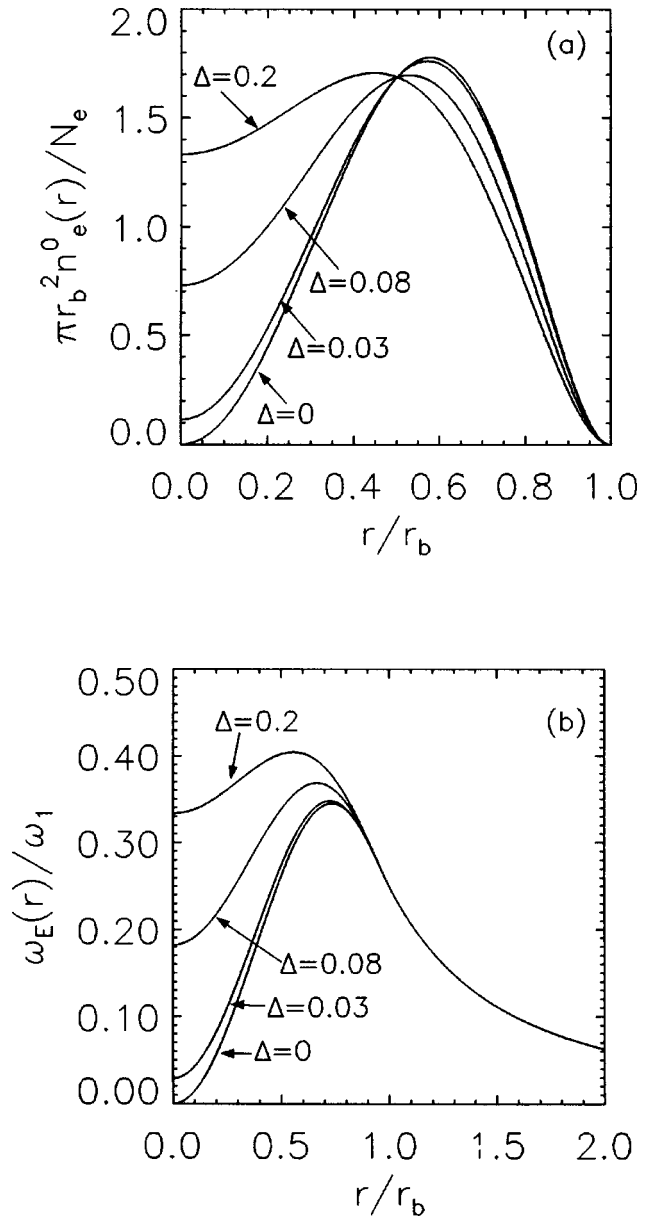


FIG. 12. Plots versus r/r_b of the normalized profiles for (a) $\pi r_b^2 n_e^0(r)/N_e$ and (b) $\omega_E(r)/\omega_1$ calculated from Eqs. (9), (10), (30) and (31) for $r_b/r_w=0.5$ and several values of the dimensionless parameter Δ corresponding to $\Delta=0, 0.03, 0.08$ and 0.2 .

lytical solutions to the eigenvalue equation (1) are not tractable as was the case for the step-function density profile treated in Sec. III A. In the subsequent analysis of Eq. (1), we make use of the numerical code developed by White²¹ for solving eigenvalue equations in planar geometry. In this regard, it is convenient to introduce the stretched radial variable X defined by

$$X = \ln\left(\frac{r}{r_b}\right), \quad \text{or} \quad \frac{r}{r_b} = \exp(X), \quad (32)$$

so that $r=0$ corresponds to $X=-\infty$, $r=r_b$ corresponds to $X=0$ and $r=r_w$ corresponds to $X=X_w \equiv \ln(r_w/r_b)$. Some straightforward algebra that makes use of Eqs. (1), (32) and $r\partial/\partial r = \partial/\partial X$ gives the transformed eigenvalue equation

$$\left[\frac{\partial^2}{\partial X^2} + F_I(X, \omega) \right] \delta\Phi_I(X) = 0. \quad (33)$$

Here, $F_I(X, \omega)$ is defined by

$$F_I(X, \omega) = -l^2 + \frac{l}{\omega - l\omega_E(X)} \frac{\partial}{\partial X} \frac{\omega_{pe}^2(X)}{\omega_{ce}}, \quad (34)$$

where $\omega_{pe}^2(X)$ and $\omega_E(X)$ are defined in Eqs. (9) and (30) with $r/r_b = \exp(X)$. The transformed eigenvalue equation (33) is solved in the two regions corresponding to the following: the plasma interior (Region I, where $0 \leq r < r_b$, or equivalently, $-\infty \leq X < 0$), and the vacuum region [Region II, where $r_b < r \leq r_w$, or equivalently $0 < X \leq X_w \equiv \ln(r_w/r_b)$]. Requiring that $\delta\Phi_I$ be regular at the origin and vanish at the conducting wall gives the boundary conditions

$$\begin{aligned} \delta\Phi_I(X \rightarrow -\infty) &= 0, \\ \left[\frac{\partial}{\partial X} \delta\Phi_I \right]_{X \rightarrow -\infty} &= 0, \end{aligned} \quad (35)$$

and

$$\delta\Phi_I^{\text{II}}(X = X_w) = 0. \quad (36)$$

In addition, for the continuously-varying density profile in Eq. (9), it is readily shown from Eqs. (33) and (34) that both $\delta\Phi_I(X)$ and $\partial\delta\Phi_I/\partial X$ are continuous across the surface of the plasma column at $X=0$ (corresponding to $r=r_b$), i.e.,

$$\begin{aligned} \delta\Phi_I(X=0) &= \delta\Phi_I^{\text{II}}(X=0), \\ \left[\frac{\partial}{\partial X} \delta\Phi_I \right]_{X=0} &= \left[\frac{\partial}{\partial X} \delta\Phi_I^{\text{II}} \right]_{X=0}. \end{aligned} \quad (37)$$

In the vacuum region, where $\omega_{pe}^2(X)=0$, Eq. (33) reduces to

$$\left[\frac{\partial^2}{\partial X^2} - l^2 \right] \delta\Phi^{\text{II}}(X) = 0, \quad 0 < X \leq X_w, \quad (38)$$

where $X_w \equiv \ln(r_w/r_b)$. Integrating Eq. (38), and enforcing $\delta\Phi_I^{\text{II}}(X = X_w) = 0$ gives the solution

$$\begin{aligned} \delta\Phi_I^{\text{II}}(X) &= \delta\Phi_b \frac{\exp[-l(X - X_w)] - \exp[l(X - X_w)]}{[\exp(lX_w) - \exp(-lX_w)]}, \\ 0 < X &\leq X_w. \end{aligned} \quad (39)$$

Here, the constant $\delta\Phi_b \equiv \delta\Phi_I(X=0)$ is the perturbed potential amplitude at the surface of the plasma column ($X=0$).

Interior to the plasma, where $\omega_{pe}^2(X)$ and $\omega_E(X)$ are specified by Eqs. (9) and (30), the eigenvalue equation (33) reduces to

$$\left[\frac{\partial^2}{\partial X^2} + F_I^{\text{I}}(X, \omega) \right] \delta\Phi_I^{\text{I}}(X) = 0, \quad -\infty \leq X < 0. \quad (40)$$

Here, $F_I^{\text{I}}(X, \omega)$ is defined by

$$\begin{aligned} F_I^{\text{I}}(X, \omega) &= -l^2 + 2\hat{\omega}_d \frac{\partial}{\partial X} \{ [\Delta + \exp(2X)][1 - \exp(2X)]^2 \} \\ &\quad \times \{ \omega - l\hat{\omega}_d [\Delta + (\tfrac{1}{2} - \Delta)\exp(2X)] \\ &\quad - \tfrac{1}{3}(2 - \Delta)\exp(4X) + \tfrac{1}{4}\exp(6X) \}^{-1}. \end{aligned} \quad (41)$$

In the present analysis, Eq. (40) is integrated numerically in Region I ($-\infty \leq X < 0$) subject to the boundary conditions in Eq. (35) at $X \rightarrow -\infty$, and the solution for $\delta\Phi_I^{\text{I}}(X)$ is matched at $X=0$ to the solution for $\delta\Phi_I^{\text{II}}(X)$ in Region II given in Eq. (39) by imposing the boundary conditions in Eq. (37). For specified values of the dimensionless parameter Δ , total amount of plasma (ω_1) and location of the conducting wall (r_b/r_w), this procedure gives numerical solutions for the eigenfunction $\delta\Phi_I(X)$ and (complex) eigenfrequency ω .

In the subsequent analysis, it should be recognized that there are significant differences between the *continuously-varying* density profile in Eq. (9) and the *step-function* density profile in Eq. (7). First, the continuously-varying density profile in Eq. (9) is very sensitive to small increases in the dimensionless parameter Δ . This is evident from Fig. 12, where Δ is varied from $\Delta=0$ to $\Delta=0.2$ at fixed values of N_e and r_b/r_w . Second, the *steep* density gradient at the inner surface $r=r_b$ in Eq. (7) (see also Fig. 1) tends to produce a strong version of the diocotron instability with sizeable growth rate $Im \omega$ measured in units of ω_1 (see Figs. 3–7). By contrast, the density gradients in Eq. (9) and Fig. 12 are *gentle*, and we find in the subsequent analysis that the growth rates of the diocotron instability are correspondingly small with $Im \omega \ll \omega_1$. Indeed, denoting the real oscillation frequency by $Re \omega = \omega_r$, it is found that a small class of *resonant* particles^{1,9,11} located at radius $r=r_s$ determined from the resonance condition

$$\omega_r - l\omega_E(r_s) = 0 \quad (42)$$

play a controlling role in determining properties of the diocotron instability for the continuously-varying density profile in Eq. (9). By contrast, for the case of the step-function density profile in Eq. (7), the diocotron instability calculated from the dispersion relation (25), which is a quadratic equation for ω , tends to be *algebraic* in nature.

Typical results obtained by numerically integrating the eigenvalue equation (40) and matching boundary conditions at $X=0$ as described earlier in this section are presented in Figs. 13 and 14 for the case where $r_b/r_w=0.5$. Shown in Fig. 13 are plots versus Δ of the normalized real oscillation frequency $Re \omega/\omega_1$ and growth rate $Im \omega/\omega_1$ of the unstable diocotron modes with azimuthal mode numbers $l=2,3,4$. It is evident from Fig. 13 that the $l=3$ mode has the largest growth rate, and that the $l=1$ mode is stable with $Im \omega=0$ and $Re \omega=\omega_1$, as expected. Moreover, from Fig. 13(b), the instability growth rate is strongest when $\Delta=0$, i.e., when the density depression in Fig. 12 is largest, and the instability growth rates decrease to negligibly small levels as Δ is increased to modest values ($\Delta \leq 0.08$). Similar behavior is evident in Fig. 14 where $Re \omega/\omega_1$ and $Im \omega/\omega_1$ are plotted versus the azimuthal mode number l for $l=1,2,\dots,7$, and values of Δ corresponding to $\Delta=0, 0.01$ and 0.03 . With regard to the linear dependence of $Re \omega$ on mode number l evident from the numerical results in Fig. 14(a), a remarkably good fit is provided by the empirical formula $Re \omega = (5l-4)\omega_1$. Finally, from Fig. 14(b), the $l=3$ mode exhibits the strongest instability, and the maximum growth rate decreases rapidly as Δ is increased to small nonzero values.

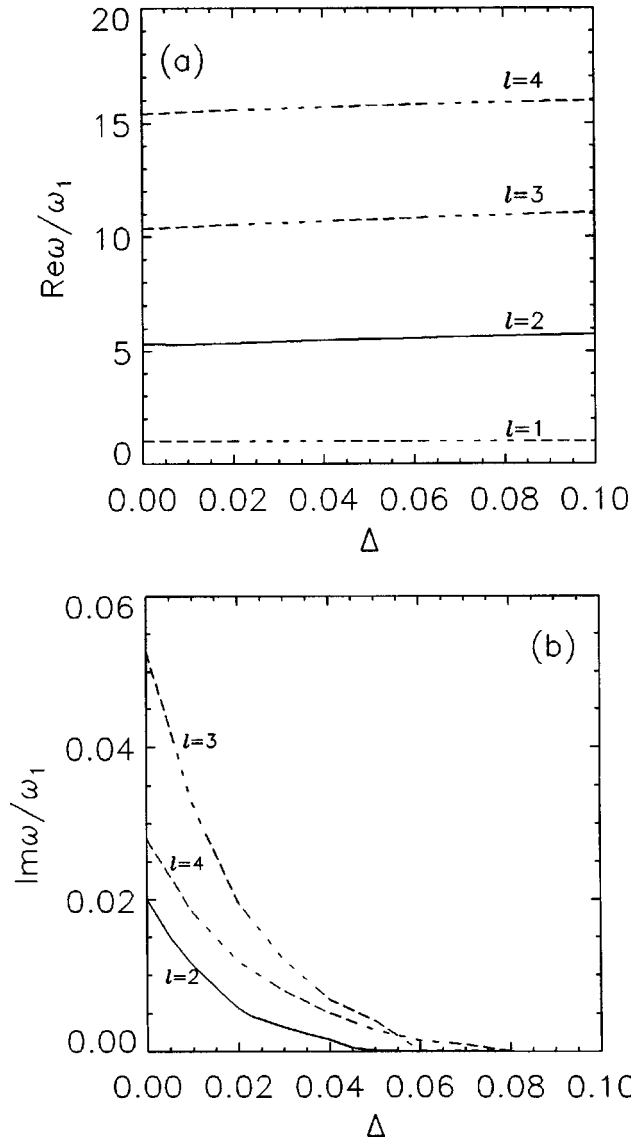


FIG. 13. Plots versus Δ of (a) the normalized real frequency $Re \omega / \omega_1$, and (b) normalized growth rate $Im \omega / \omega_1$ obtained numerically for the choice of continuously-varying density profile in Eq. (9). Here, $r_b/r_w=0.5$ is assumed, and results are presented for mode numbers $l=1, 2, 3, 4$.

Typical numerical results obtained for the radial dependence of the complex eigenfunction are illustrated in Figs. 15 and 16 for the choice of system parameters $\Delta=0$ and $r_b/r_w=0.5$ (see Fig. 14 for the corresponding values of $Re \omega$ and $Im \omega$). The most natural (but perhaps least informative) representation of the eigenfunction is in terms of the perturbed electrostatic potential, which is shown in Fig. 15 for azimuthal mode number $l=2$. As expected, $\delta\Phi_l(r)$ has both real and imaginary parts in Fig. 15, and the eigenfunction has a broad radial structure with maximum magnitude where the plasma density is large. Because the eigenvalue equation (1) is homogeneous in the complex eigenfunction $\delta\Phi_l(r)$, it should be noted that $\delta\Phi_l(r)$ can be scaled by a factor $\exp(i\alpha)$, where α is a constant phase factor. In Fig. 15, when integrating Eq. (1) [or equivalently, Eq. (33)], we have chosen the phase α so that the eigenfunction $\delta\Phi_l(r)$ is purely real for small values of r near the origin. A careful

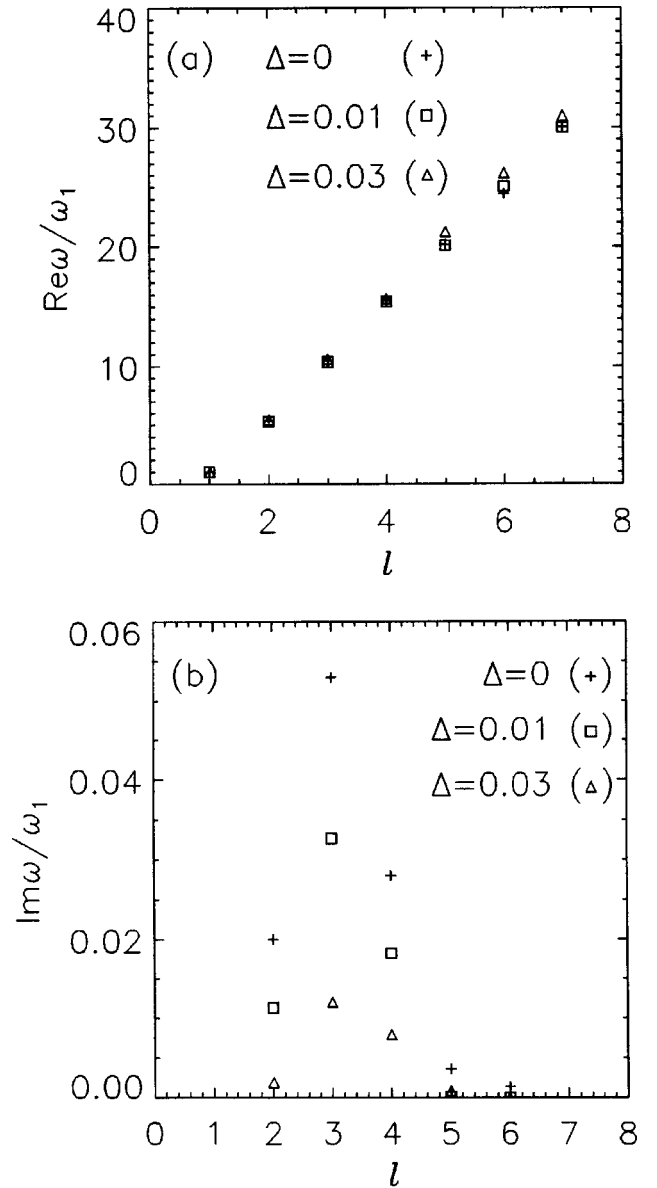


FIG. 14. Plots versus azimuthal mode number l of (a) the normalized real frequency $Re \omega / \omega_1$, and (b) the normalized growth rate $Im \omega / \omega_1$ obtained numerically for the choice of a continuously-varying density profile in Eq. (9). Here, $r_b/r_w=0.5$ is assumed, and results are presented for $\Delta=0, 0.01$ and 0.03 .

examination of Eq. (1) for small r then shows that $[r^{-1}(\partial/\partial r)(r\partial/\partial r) - l^2/r^2]Im \delta\Phi_l(r)$ is proportional to $[r^{-1}\partial\omega_p^2/\partial r]_{\omega_r=l\omega_E(r)}Re \delta\Phi_l(r)$. Therefore, as evident from Fig. 15, $Im \delta\Phi_l(r)$ vanishes until r increases to r_s , the resonant radius that solves $\omega_r=l\omega_E(r_s)$.

As shown in Fig. 16, for mode numbers $l=2, 3$ and 4 , it is much more informative to plot the real and imaginary parts of the eigenfunction for the perturbed density $\delta n_l(r) = (4\pi e)^{-1}[r^{-1}(\partial/\partial r)(r\partial\delta\Phi_l/\partial r) - (l^2/r^2)\delta\Phi_l]$. Evidently, for each value of $l=2, 3$ and 4 , both $Re \delta n_l(r)$ and $Im \delta n_l(r)$ are very strongly peaked in a narrow radial region of the positive density gradient. Indeed, from the numerical solutions for $Re \omega = \omega_r$, it is found that the precise radial location $r=r_s$ of the localized density perturbation in Fig. 16 is determined from the resonance condition $\omega_r - l\omega_E(r_s)$

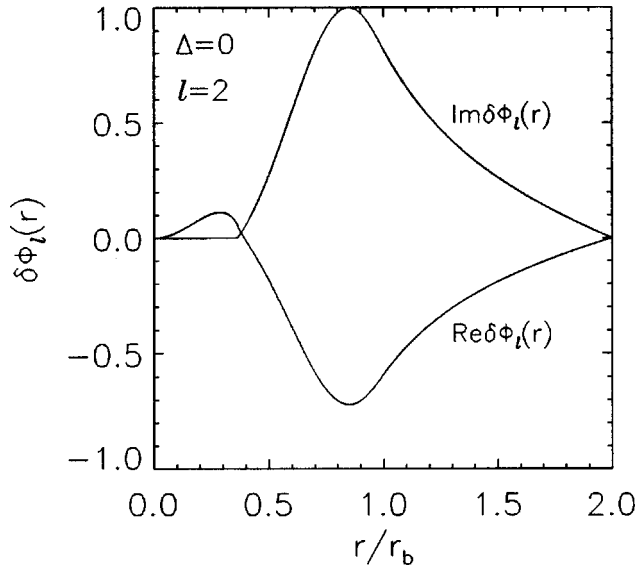


FIG. 15. Plots of $\text{Re } \delta\Phi_l(r)$ and $\text{Im } \delta\Phi_l(r)$ versus r/r_b obtained numerically for $\Delta=0$ and $l=2$ for the choice of a continuously-varying density profile in Eq. (9). Here, $r_b/r_w=0.5$ is assumed.

$=0$ in Eq. (42), where $\omega_E(r)$ is the angular velocity profile defined in Eq. (30). (Here, $\Delta=0$ and $r_b/r_w=0.5$ for the plots in Fig. 16.)

Note also from Fig. 16 that as l increases from $l=2$ to $l=3$ to $l=4$, the resonant radius $r=r_s$ moves progressively outwards towards the density maximum at $r_{\text{max}}/r_b=(1/3)^{1/2}=0.577$ (for $\Delta=0$). This is further illustrated in Fig. 17 where the values of r_s calculated numerically from Eqs. (30) and (42) and the numerical solutions for ω_r are plotted for mode numbers $l=1,2,\dots,10$. In Fig. 17, the values of r_s to the right of the density maximum but to the left of r_b correspond to purely oscillatory modes with $\text{Im } \omega=0$ and mode numbers $l=6,\dots,10$. For values of r_s in Fig. 17 to the left of the density maximum, the $l=1$ mode, of course, is a stable oscillation with $\text{Im } \omega=0$ and $\text{Re } \omega=\omega_1$, whereas the $l=2,3,\dots$ modes are unstable, with largest growth rate for $l=3$, and a negligibly small growth rate for $l\geq 7$ (see Fig. 14). Finally, it should also be pointed out in Fig. 16 that the real and imaginary parts of the eigenfunction $\delta n_l(r)$ satisfy charge conservation, $\int_0^{r_b} dr r \delta n_l(r) = 0$, as expected.

For the continuously-varying density profile specified by Eq. (9), it is evident from Figs. 13, 14 and 16, that the diocotron instability is both weak ($\text{Im } \omega \ll |\text{Re } \omega|$) and resonant. Therefore, to better understand semi-quantitative features of the instability, it is useful to summarize briefly a formulation of the *resonant* diocotron instability^{1,9,11} developed originally by Briggs *et al.*⁹ We denote $\omega_r = \text{Re } \omega$ and $\gamma = \text{Im } \omega$, and Taylor expand the effective dispersion relation $D(\omega_r + i\gamma) = 0$ in Eq. (4) for $|\gamma/\omega_r| \ll 1$. This gives

$$D(\omega_r + i\gamma) = D_r(\omega_r) + i \left[D_i(\omega_r) + \gamma \frac{\partial D_r(\omega_r)}{\partial \omega_r} \right] + \dots = 0, \quad (43)$$

where $D_r(\omega_r) \equiv \text{Re } D(\omega_r)$ and $D_i(\omega_r) \equiv \text{Im } D(\omega_r)$. Setting real and imaginary parts in Eq. (43) separately equal to zero then gives

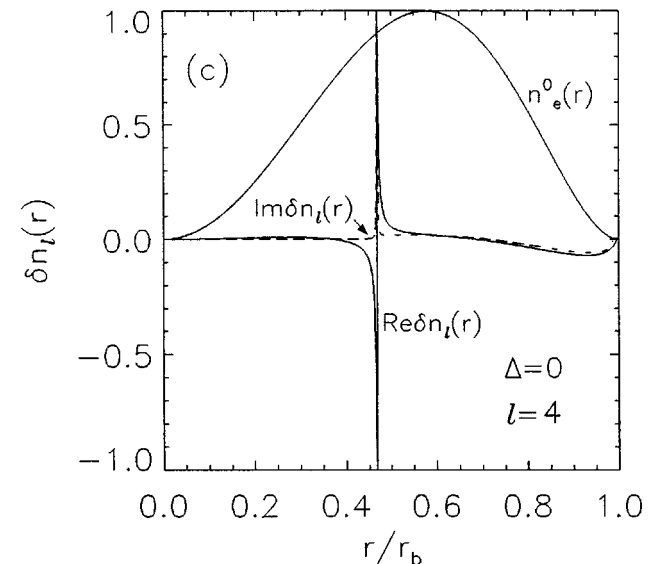
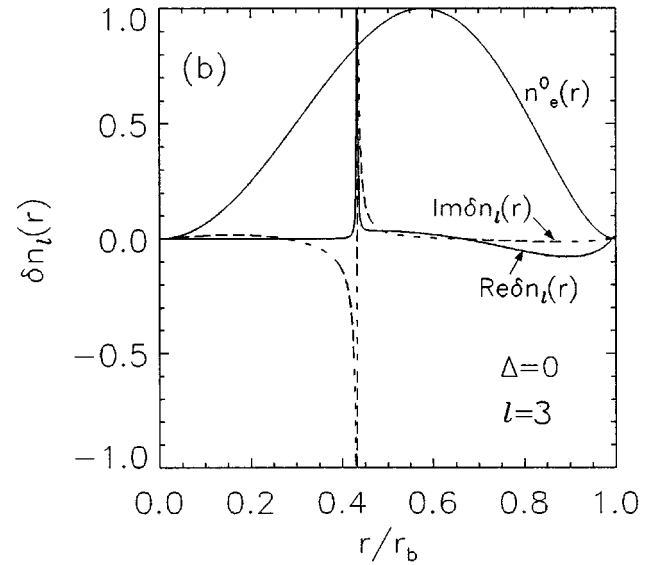
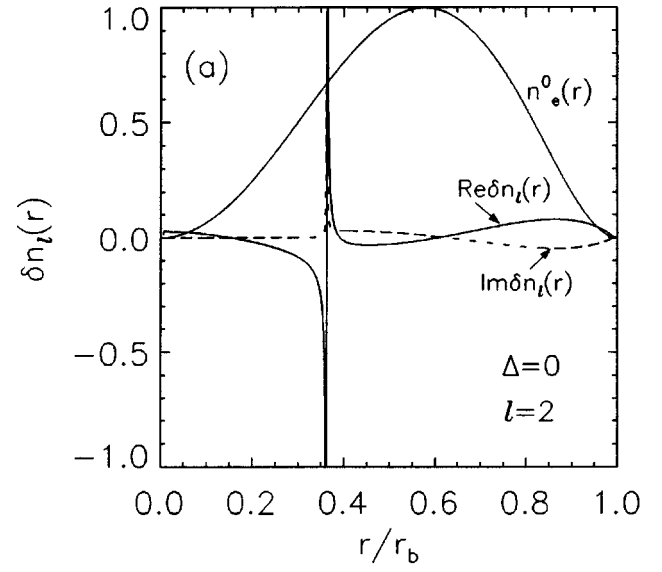


FIG. 16. Plots of $\text{Re } \delta n_l(r)$ and $\text{Im } \delta n_l(r)$ versus r/r_b obtained numerically for $\Delta=0$ and $r_b/r_w=0.5$ for azimuthal mode numbers (a) $l=2$, (b) $l=3$ and (c) $l=4$. The continuously-varying density profile $n_e^0(r)$ in Eq. (9) is also plotted versus r/r_b in the figures.

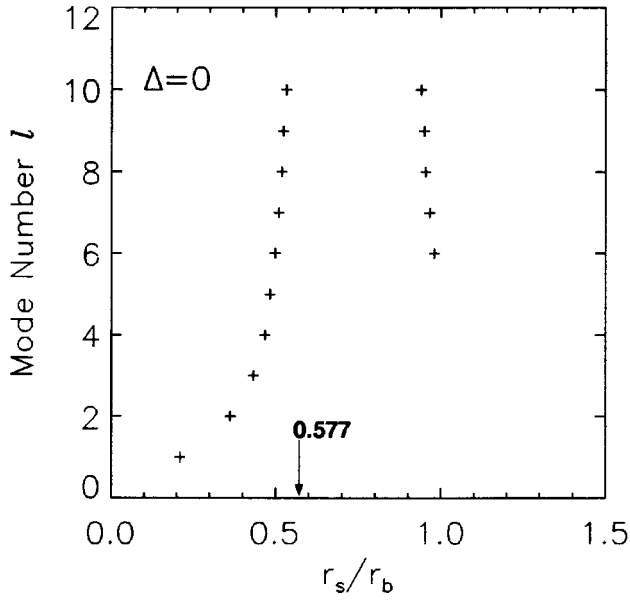


FIG. 17. Plots for $\Delta=0$ and $r_b/r_w=0.5$ of the resonant radius r_s calculated from $\omega_r - l\omega_E(r_s) = 0$ for azimuthal mode numbers $l=1,2,\dots,10$, and values of r_s located within the plasma ($0 < r_s < r_b$). Here, the density profile $n_e^0(r)$ and angular velocity profile $\omega_E(r)$ are specified by Eqs. (9) and (30), and $\omega_r = Re \omega$ is determined numerically from the eigenvalue equation.

$$D_r(\omega_r) = 0, \quad (44)$$

$$\gamma = - \frac{D_i(\omega_r)}{\partial D_r(\omega_r) / \partial \omega_r}.$$

To evaluate $D_r(\omega_r)$ and $D_i(\omega_r)$, we make use of

$$\lim_{\gamma \rightarrow 0+} \frac{1}{\omega_r - l\omega_E(r) + i\gamma} = \frac{P}{\omega_r - l\omega_E(r)} - i\pi \delta[\omega_r - l\omega_E(r)] \quad (45)$$

in Eq. (4), where P denotes Cauchy principal value. Substituting Eq. (45) into Eq. (4) and taking the limit $\gamma \rightarrow 0+$ then gives

$$D_r(\omega_r) = \int_0^{r_w} dr r \left\{ \left| \frac{\partial}{\partial r} \delta\Phi_l \right|^2 + \frac{l^2}{r^2} |\delta\Phi_l|^2 - \frac{l}{r\omega_{ce}} \frac{P \partial \omega_{pe}^2 / \partial r}{\omega_r - l\omega_E(r)} |\delta\Phi_l|^2 \right\}, \quad (46)$$

and

$$D_i(\omega_r) = \frac{l}{\omega_{ce}} \pi \int_0^{r_w} dr \frac{\partial}{\partial r} \omega_{pe}^2(r) \delta[\omega_r - l\omega_E(r)] |\delta\Phi_l|^2 = \frac{\pi}{\omega_{ce}} \left[\frac{\partial \omega_{pe}^2(r) / \partial r |\delta\Phi_l|^2}{|\partial \omega_E(r) / \partial r|} \right]_{r=r_s}, \quad (47)$$

where the resonant radius r_s solves $\omega_r = l\omega_E(r_s)$. Substituting Eqs. (46) and (47) into Eq. (44) then gives¹

$$0 = D_r(\omega_r) = \int_0^{r_w} dr r \left\{ \left| \frac{\partial}{\partial r} \delta\Phi_l \right|^2 + \frac{l^2}{r^2} |\delta\Phi_l|^2 - \frac{l}{\omega_{ce}} \frac{P \partial \omega_{pe}^2 / \partial r}{\omega_r - l\omega_E(r)} |\delta\Phi_l|^2 \right\}, \quad (48)$$

and

$$\gamma = \frac{\pi}{l} \left[\frac{\partial \omega_{pe}^2(r) / \partial r |\delta\Phi_l|^2}{|\partial \omega_E(r) / \partial r|} \right]_{r=r_s} \times \left[- \int_0^{r_w} dr \frac{P \partial \omega_{pe}^2 / \partial r}{(\omega_r - l\omega_E)^2} |\delta\Phi_l|^2 \right]^{-1}. \quad (49)$$

Equation (48) plays the role of a dispersion relation¹ for the real oscillation frequency ω_r , whereas Eq. (49) determines the growth rate γ of the resonant diocotron instability. Of course neither Eq. (48) nor Eq. (49) provide information on the detailed functional form of the complex eigenfunction $\delta\Phi_l(r)$. Nonetheless, important qualitative features of the instability are evident. In particular, for the continuously-varying density profile in Eq. (9), the factor $[\dots]^{-1}$ in Eq. (49) is positive, so that the positive density gradient factor $[\partial \omega_{pe}^2 / \partial r]_{r=r_s}$ drives the resonant diocotron instability for values of the resonant radius r_s to the left of the density maximum.

IV. CONCLUSIONS

In this paper, we have made use of the electrostatic eigenvalue equation (1) to determine the influence of density profile shape on the diocotron instability in a low-density ($\omega_{pe}^2 \ll \omega_{ce}^2$) non-neutral plasma column confined by a uniform axial magnetic field $B_0 \hat{e}_z$. The assumptions and theoretical model were described in Sec. II, and in Sec. III detailed stability results were presented for two classes of equilibrium density profiles $n_e^0(r)$ with inverted population as a function of radius r . The first (Sec. III A) corresponds to the step-function density profile in Eq. (7) (see Fig. 1), whereas the second (Sec. III B) corresponds to the continuously-varying density profile in Eq. (9) (see Figs. 2 and 12). In both cases, the dimensionless parameter Δ controls the degree of “hollowness” of the equilibrium density profile, with $\Delta=0$ corresponding to $n_e^0(r=0)=0$. Detailed stability properties were calculated in Sec. III for a wide range of system parameters, including values of Δ , radial location r_w of the conducting wall, azimuthal mode number l , etc. As a general remark, in both cases, it was shown that small increases in the “filling factor” Δ from the value $\Delta=0$ can have a large effect on the growth rate and detailed properties of the instability. In addition, for the step-function density profile in Eq. (7), which has a steep density gradient at the inner layer surface ($r=r_b^-$), the instability tends to be algebraic in nature and have a large growth rate in the unstable region of parameter space (see Figs. 3–7). By contrast, for the continuously-varying density profile in Eq. (9), the instability is typically much weaker (see Figs. 13 and 14) and involves a narrow class of resonant particles at radius $r=r_s$ satisfying the resonance condition in Eq. (42). To help better understand the qualitative features of the weak resonant dio-

cotron instability, an expression for the growth rate $\gamma = \text{Im } \omega$ was presented in Eq. (49), which relates the growth rate γ directly to the density gradient $\partial \omega_{pe}^2(r)/\partial r$ at the resonant radius $r = r_s$.

In conclusion, to help motivate future experimental studies, the present analysis has quantified the sensitive dependence of the diocotron instability growth rate and mode structure on the shape of the equilibrium density profile $n_e^0(r)$. Detailed stability properties have been calculated for profiles ranging from a thin annulus to a continuously varying density profile with inverted population. It is hoped that this work will motivate future experimental studies, both to test the validity of the linear stability analysis, and to help guide the planning of experiments to preferentially excite certain modes (l -values) and follow their nonlinear evolution. In this regard, it is important to note that the perturbed density $\delta n_l(r)$, rather than the perturbed potential $\delta \phi_l(r)$, is a particularly sensitive diagnostic of the detailed mode structure.

ACKNOWLEDGMENTS

It is a pleasure to thank Roscoe White for useful discussions in implementing the numerical scheme to solve the eigenvalue equation in Sec. III.

This research was supported by the Office of Naval Research, and in part by the Department of Energy.

- ¹R. C. Davidson, *Physics of Nonneutral Plasmas* (Addison-Wesley, Reading, MA, 1990), pp. 289–343, and references therein.
- ²C. C. MacFarlane and H. G. Hay, Proc. Phys. Soc. London, Sect. B **63**, 409 (1950).
- ³R. H. Levy, Phys. Fluids **8**, 1288 (1965).
- ⁴R. H. Levy, Phys. Fluids **11**, 920 (1968).
- ⁵O. Buneman, R. H. Levy, and L. M. Linson, J. Appl. Phys. **37**, 3203 (1966).
- ⁶R. L. Kyhl and H. F. Webster, IRE Trans. Electron Devices **ED-3**, 172 (1956).
- ⁷H. F. Webster, J. Appl. Phys. **26**, 1386 (1955).
- ⁸C. A. Kapetanakis, D. A. Hammer, C. Striffler, and R. C. Davidson, Phys. Rev. Lett. **30**, 1303 (1973).
- ⁹R. J. Briggs, J. D. Daugherty, and R. H. Levy, Phys. Fluids **13**, 421 (1970).
- ¹⁰R. C. Davidson, Phys. Fluids **27**, 1804 (1984).
- ¹¹R. C. Davidson, Phys. Fluids **28**, 1937 (1985).
- ¹²T. M. O'Neil and R. A. Smith, Phys. Fluids B **4**, 2720 (1992).
- ¹³G. Rosenthal, G. Dimonte, and A. Y. Wong, Phys. Fluids **30**, 3257 (1987).
- ¹⁴K. S. Fine, C. F. Driscoll, and J. H. Malmberg, Phys. Rev. Lett. **63**, 2232 (1989).
- ¹⁵C. F. Driscoll and K. S. Fine, Phys. Fluids B **2**, 1359 (1990).
- ¹⁶C. F. Driscoll, Phys. Rev. Lett. **64**, 645 (1990).
- ¹⁷X.-P. Huang and C. F. Driscoll, Phys. Rev. Lett. **72**, 2187 (1994).
- ¹⁸K. S. Fine, A. C. Cass, W. G. Flynn, and C. F. Driscoll, Phys. Rev. Lett. **75**, 3277 (1995).
- ¹⁹R. C. Davidson, H.-W. Chan, C. Chen, and S. Lund, Rev. Mod. Phys. **63**, 341 (1991).
- ²⁰D. J. Kaup and G. E. Thomas, J. Appl. Phys. **71**, 5752 (1992).
- ²¹R. B. White, J. Comput. Phys. **31**, 409 (1979).